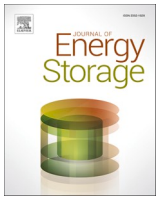
Journal of Energy Storage 183 (2027) 125322



Contents lists available at ScienceDirect

Journal of Energy Storage

journal homepage: www.elsevier.com/locate/est



Research papers

Multi-objective optimisation of slit casing geometries in flywheel energy storage systems

Mahmoud Eltaweel, Mohammad Reza Herfatmanesh *

School of Physics, Engineering and Computer Science, University of Hertfordshire, Hatfield, AL10 9AB, United Kingdom

ARTICLE INFO

Keywords:
Energy recovery system
Response surface methodology
Flywheel energy storage systems
Taylor-Couette flow
Windage losses
Nusselt number

ABSTRACT

Amidst the current need for sustainable and effective energy storage solutions, flywheel energy storage systems (FESS) have emerged as viable options to meet the dynamic energy demands of modern society. This study employs Computational Fluid Dynamics (CFD) simulations, integrated with Response Surface Methodology (RSM), to pinpoint the optimal design parameters that govern annular flow in these systems, thereby influencing windage losses and heat transfer properties. A comprehensive analysis was conducted across four distinct geometries, scrutinising design variables such as rotational velocity, internal pressure, slit geometry, slit base-to-height ratio, and slit wall. Through Analysis of Variance (ANOVA), the study revealed significant interdependencies between these examined parameters. Results indicate that by optimising operational conditions within the FESS, windage losses can be decreased by 8% and heat transfer, as measured by the Nusselt number, can be improved by 11% compared to the initial model. The research determines several optimum design values based on windage losses and heat transfer significance, offering a pathway to substantially elevate the performance and reliability of FESS units. The findings of this study could make a substantial contribution to advancing guidelines for optimising the design of FESS in the energy sector.

1. Introduction

Flywheel Energy Storage Systems (FESS) have emerged as promising solutions for handling modern society's dynamic energy needs in an era marked by an increasing demand for sustainable and efficient energy storage systems [1]. FESS uses rotational energy storage concepts to provide a dependable and high-performance technique of storing and releasing energy [2]. A flywheel rotor is a mechanical component that rotates at a specific speed and mass and can store energy due to its speed and mass [3]. As technology has advanced, researchers and engineers have been actively seeking new solutions to enhance the operational capabilities of these systems. Concurrently, there has been a strong focus on improving the performance of FESS [4].

One of the key challenges in the realm of FESS optimisation is the mitigation of windage losses within the system [5]. Windage loss is caused by frictional effects between the spinning component (rotor) and the surrounding gas (air), which results in energy dissipation in the form of heat [6]. Windage loss contributes significantly to total losses in high-speed rotating machines such as flywheels, increasing self-discharge, which can significantly impair FESS' overall efficiency and effectiveness [7]. As a result, windage loss may render FESS unsuitable for medium-term energy storage applications [8].

The total windage loss of the rotor is the sum of three parameters. The first is the viscous shear generated on the cylindrical lateral surface of the rotor, which arises from the azimuthal velocity gradient sustained across the radial airgap and is quantified through the rotor skin friction coefficient; in a narrow-gap, high-aspect-ratio machine of the type considered here, this is the dominant contribution. The second is the frictional loss generated on the two rotor end faces, which behave as enclosed rotor–stator disc cavities and are characterised by a disc torque coefficient. The third is the form, or pressure, drag associated with geometric discontinuities on the bounding surfaces, such as the casing slits examined in this study; this contribution is absent from a smooth annulus and manifests itself as a modification of the two preceding coefficients rather than as an independent term. A fourth contribution, the ventilation loss associated with an imposed axial through-flow, arises in machines with forced cooling but is absent from the sealed configuration considered here. The first two contributions correspond to the two terms of the windage power expression introduced in Section 2.2 and are evaluated separately from the computational solution throughout this

* Corresponding author.
E-mail address: m.r.herfatmanesh@herts.ac.uk (M.R. Herfatmanesh).

https://doi.org/10.1016/j.est.2026.125322
Received 19 May 2026; Received in revised form 23 September 2026; Accepted 24 October 2026
Available online 30 October 2026
2352-152X/© 2026 The Authors. Published by Elsevier Ltd. This is an open access article under the CC BY license (http://creativecommons.org/licenses/by/4.0/).

work.

The same annular flow that generates the frictional loss also governs the convective transport of the dissipated heat from the rotor to the casing, and the rotor temperature that results determines both the material limit on rotational speed and the temperature-dependent properties of the enclosed gas. Windage loss and the Nusselt number therefore cannot be optimised independently, which is the reason both are retained as responses in the optimisation framework described in Section 3.

The prevailing industrial response to windage loss is to create partial vacuum in the containment vessel, and commercial flywheel installations routinely operate at internal pressures well below atmospheric. Although this is an effective solution, it is not without penalty. It requires a vacuum pump and its associated parasitic power, a high-integrity rotating seal and feedthrough arrangement, materials and lubricants selected for low outgassing, and periodic re-evacuation to compensate for leakage, all of which increase capital cost, part count and maintenance burden. A further consequence is thermal: as the gas is removed, the convective path by which heat is transported from the rotor to the casing is progressively suppressed, so that the rotor rejects heat almost exclusively by radiation and its temperature, rather than its windage loss, becomes the limiting constraint.

The design question addressed in this study is therefore whether the losses that remain at moderate sub-atmospheric and ambient pressures can be reduced by geometric means alone, so that the depth of vacuum required, and with it the complexity and cost of the containment system, may be relaxed while the convective cooling path to the rotor is retained. The pressure range examined in this study, 0.2 to 1 bar, spans rough vacuum to fully ambient operation and is representative of the cost-driven, seal-tolerant flywheel installations developed for automotive and short-duration grid support duty, for which the elimination of a continuously operating vacuum system is of greater value than maximum windage loss reduction. The practical relevance of this design space was established in discussion with the industrial partner associated with the authors' earlier experimental work [5].

A typical flywheel comprises an outer fixed cylinder and a rotating inner cylinder, a configuration known as Taylor-Couette flow. Taylor vortices emerge in this flow when the rotational speed crosses a particular threshold, which in turn affects the system's flow dynamics [9]. Researchers have been exploring means to enhance heat transfer which would reduce windage losses in Taylor-Couette flow through various design modifications. Some have studied the impact of altering slit geometry to improve heat transfer [10], while others have investigated how structural parameters could be adjusted for the same purpose [11]. Further, Tsukahara et al. [12] have shed light on the effects of rib orientation and spacing on flow resistance.

Additional research in the field has looked into the role of groove configurations in heat transfer. Findings from these studies have pointed to the effectiveness of helical fins over their longitudinal counterparts [13]. Other experiments have quantified the improvement in heat transfer rates in grooved channels, underscoring the potential for implementing such features in high-speed rotating machines [14].

Liu et al. [15] [16] analysed the turbulent Taylor-Couette flow in a slit model, highlighting that slit dimensions affect flow distribution and heat transfer. Increased slit width and number notably enhance heat transfer, and Reynolds number has a significant impact on the slit wall structure. Further investigations from Liu et al. [17] with varying Reynolds numbers and temperature gradients revealed enhancements in heat transfer and flow transition under diverse conditions.

Sun et al. [10] studied slit structure designs in coaxial cylinders using large eddy modelling. The elliptical slit design proved superior in heat transfer efficiency, owing to effective fluid exchange and minimal entropy creation. Sommerer and Lauriat [18] found that the number of rectangular slits significantly influences heat transfer, while Zhu et al. [19] studied V-shaped slits, finding them ineffective if the slit depth is below the boundary layer thickness. Liu et al. [20] again demonstrated that slit wall shapes, particularly trapezoid cross-sections, had a substantial impact on flow distribution and heat transfer. Other studies have focused on groove geometry, confirming that distinct configurations affect pressure drop and heat transfer rates differently [21] [22] [23].

In the realm of flow types, Tachibana and Fukui [24] found that grooves delay the onset of Taylor vortices, effectively increasing the critical Taylor number. Lee et al. [25] documented five distinct types of flow in Taylor-Couette setups. Eiamsa-ard and Promvonge [26] established that all groove shapes enhance heat transfer rates compared to a smooth channel. The utility of Response Surface Methodology (RSM) for analysing complex experiments has also been demonstrated [27]. Salviano et al. [28] optimised heat transfer performance of plate-fin heat exchangers using RSM, while Nouri-borujerdi and Nakhchi [29] used it to pinpoint influential design parameters for annular flow. Lastly, Sun et al. [11] employed RSM to optimise Taylor-Couette flow, finding that increased Reynolds numbers and slit widths significantly improved heat transfer.

The potential of incorporating slit designs to diminish windage losses within FESS has not been previously explored in the literature. Although such designs have been acknowledged for their efficacy in enhancing heat transfer capabilities, the specific impact of slit incorporation on the performance optimisation of FESS remains an uncharted area of research. This study aims to fill that gap by investigating how slit designs can be leveraged to not only improve heat dissipation but also to potentially reduce windage losses, thereby contributing to the overall efficiency of the system.

Although the influence of slit and groove geometries on Taylor–Couette flow has been examined extensively, the existing body of work is bounded in three respects. First, heat transfer enhancement has almost invariably been treated as the sole objective, with the associated torque or frictional penalty either not reported or reported only as a secondary observation, so that the trade-off between the two has not been assessed. Second, the parameter space explored within individual studies has been narrow, typically comprising a single cross-sectional profile with the slit number or width varied over a small number of levels, so that the interactions between profile shape, aspect ratio, orientation and the manner in which the slit is realised in the casing have remained inaccessible. Third, the operating envelope considered has been that of a laboratory Taylor–Couette apparatus rather than that of a high-speed energy storage machine, in which the peripheral velocity, the sub-atmospheric operating pressure and the coupling between rotor temperature and self-discharge are each of first-order importance.

The contribution of the present work is twofold, and the distinction between its two aspects is made explicit here. Methodologically, this study constitutes the most extensive parametric treatment of slit walls in Taylor–Couette flow reported to date: the cross-sectional profile, the base length-to-height ratio, the orientation of the slit relative to the axis of rotation and the configuration by which the slit is formed in the casing are varied simultaneously, at a constant slit wall area, and their individual and combined effects are quantified by analysis of variance within a single response surface framework. The combined effect of these factors, and in particular the interaction between slit orientation and slit configuration that emerges as one of the strongest terms in the analysis, has not previously been established. In terms of application, this is, to the best of the authors' knowledge, the first study in which casing slit geometries are optimised against windage loss in a flywheel energy storage system, and the first in which windage loss and convective heat transfer are treated as competing objectives within a common multi-objective optimisation.

This research aims to optimise FESS performance through the introduction of slit walls in the casing. Various slit geometries, such as rectangle and trapezoid, will be investigated to minimise windage losses and enhance heat transfer rates. The study maintains a constant slit wall area to ensure controlled comparisons across all configurations, while exploring a multi-dimensional parameter space encompassing five key

variables: rotational velocity, internal pressure, slit geometry, base length-to-height ratio, and slit wall configuration. Through the application of RSM, numerical simulations and data analysis are carried out to characterise the influence of slit geometries on flow field distribution, heat transfer, and windage losses. To the best of the authors' knowledge, this constitutes the first investigation into the effect of casing slit geometries on windage loss reduction in a flywheel energy storage system. The research not only offers insights for improving FESS but also contributes to broader sustainable energy goals by potentially reducing standby losses and increasing system longevity.

2. Numerical modelling

2.1. Governing equations and assumptions

This study aims to develop a numerical model for a FESS incorporating a smooth, narrow, and enclosed airgap configuration. The CFD approach is adopted to evaluate key parameters, including the skin friction coefficient, disc torque, and heat transfer coefficient, by simulating the flow behaviour within the airgap. The governing equations underpinning the CFD framework are derived from the fundamental conservation laws of fluid mechanics [30]. A computational domain representative of an enclosed FESS is established and subsequently discretised into a structured mesh of computational cells and nodal points. Following mesh generation, the governing equations are converted into a system of linear algebraic equations through numerical discretisation using the finite volume method [31]. The mass conservation principle in fluid flow is expressed through the continuity equation, presented in Eq. (1) [30].

$$\frac{\partial \rho}{\partial t} + \nabla . \rho V = 0 \tag{1}$$

In accordance with Newton's second law applied to fluid mechanics, the rate of change of momentum within a fluid element equals the net forces acting on that element, as expressed in Eq. (2) [32].

$$\frac{D(\rho V)}{Dt} = -\nabla p + \nabla \bullet \tau_{ij} + \rho g \tag{2}$$

Eq. (3) serves as the basis from which the energy equation governing compressible, viscous Newtonian fluid flow is derived [32].

$$\frac{D(\rho C_p T)}{Dt} = \nabla \bullet (\lambda \nabla T) + \Phi \tag{3}$$

Where V denotes the velocity vector, ∇p represents the pressure force, $\nabla \bullet \tau_{ij}$ is the viscous force, ρg is the gravitational force, $\nabla \bullet (\lambda \nabla T)$ refers to the heat conducted across the boundaries of the fluid element, λ is the thermal conductivity, T is the temperature and Φ accounts for the heat generated through the conversion of mechanical energy.

2.2. Flow characterisations

Couette flow is characterised as the fluid motion within the annulus of concentric cylinders, where the inner cylinder is subjected to rotational motion while the outer cylinder remains stationary. This occurs when two parallel surfaces, separated by a fluid medium, engage in consistent and relative motion [33]. The flow regime is categorised by the Knudsen number; specifically, the Navier-Stokes momentum equations depict the flow conditions for a linear Newtonian viscous fluid in instances where the Knudsen number is less than 0.01 within the fluid domain [34]. The Navier-Stokes equations are derived under the assumption that the fluid behaves as a continuous medium, and that the viscous shear stresses are linearly related to the strain rates. In the context of FESS, windage losses are induced due to viscous friction between the rotating inner cylinder (the rotor) and the fluid present in the airgap. The extent of these windage losses is generally dictated by the velocity field of the air within the airgap, which in turn is modulated by factors such as tangential air flow and Taylor-Couette phenomena. The quantification of windage losses can be carried out through an examination of airflow dynamics within the airgap. Eq. (4) serves as a mathematical representation to compute the power necessitated by the system to counteract the windage losses generated by the rotating cylinder [35].

$$P_w = \pi \rho \omega^3 {r_o}^4 L C_w + \rho \omega^3 {r_o}^5 C_m \tag{4}$$

Where ω is the rotational velocity of the rotor, ρ is the fluid density, L is the rotor length, r_o is the rotor radius, C_w is the rotor skin friction coefficient, and C_m is the disc torque coefficient.

The two terms of Eq. (4) are evaluated independently throughout this work. The first term represents the loss generated on the cylindrical lateral surface of the rotor and is obtained from the area-averaged wall shear stress computed on that surface; the second term represents the loss generated on the two rotor end faces, which are treated as enclosed rotor–stator disc cavities, and is obtained from the area-averaged wall shear stress computed on the end faces. The two coefficients are extracted separately from the converged solution and combined according to Eq. (4) to give the total windage loss. For the baseline with no slit at 2400 rad/s and ambient pressure, the cylindrical surface accounts for 82.6% of the total loss and the two end faces for the remaining 17.4%. Across the operating envelope examined the end-face share of the baseline lies between 17.3% and 18.7%. Averaged over the 240 slit configurations of the design matrix, the loss due to two end faces is 16.2%, with a range of 10.4% to 19.6%. The end-face contribution is therefore not negligible, but neither is it the dominant term.

The slits are confined to the cylindrical portion of the casing bore and terminate before the axial clearance between the rotor end faces and the casing end walls, so that the end-face geometry is identical in every configuration considered and no slit-induced disturbance acts directly upon the end-face boundary layers. The disc torque coefficient is nevertheless not invariant, because the enclosed air is common to both regions: a configuration that suppresses convective transport within the annulus raises the temperature of the enclosed air, which alters its density and kinematic viscosity and hence the local rotational Reynolds number of the rotor–stator disc cavities. This indirect coupling is evident in the results. At a fixed rotational velocity and pressure, the disc torque coefficient correlates with the mean temperature of the enclosed air with a correlation coefficient of 0.98, and with the cylindrical skin friction coefficient with a correlation coefficient of 0.96, which is the signature of a shared thermal cause rather than of a direct hydrodynamic disturbance of the end-face flow.

The magnitude of the effect on the end-face term is correspondingly smaller than that on the cylindrical term. At a representative operating point of 1800 rad/s and 0.6 bar, changing the slit configuration from grooved to inserts raises the cylindrical skin friction coefficient by 56% but the disc torque coefficient by only 18%, and changing the slit orientation from radial to axial raises them by 53% and 21%, respectively. The slit cross-sectional profile, which is the geometric factor of principal interest here, changes neither coefficient by more than 7%. The slit-induced disturbances discussed in Section 4 therefore act predominantly on the first term of Eq. (4), and the ranking of the configurations by total windage loss is governed by that term. The second term is retained in every case since it accounts for approximately one sixth of the total loss and that the absolute values reported here remain directly comparable with experimental measurements, in which the two contributions cannot be separated.

In an enclosed cylindrical geometry with no axial flow, the laminar flow regime between the cylinders becomes unstable at certain angular velocities, giving rise to a series of circumferential Taylor vortices [36]. The Couette flow is unstable with an inner rotating cylinder and an out cylinder at rest, according to the traditional invisible criterion of rotational stability. When the clearance of the cylinder airgap is minimal in

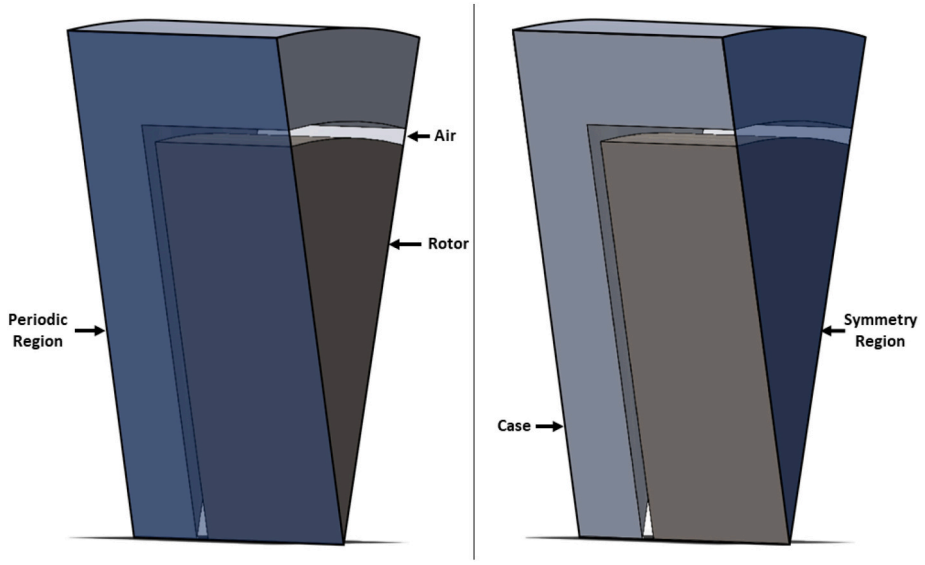


Fig. 1. Simplified geometry of FESS with periodic regions and symmetry plane.

comparison to the cylinder radius, the stable flow is determined by the Taylor number, which is given by Eq. (5) [37].

$$T_a = \frac{\omega \times r_o \times g}{\upsilon}\left(\frac{g}{r_o}\right)^{0.5} \tag{5}$$

Where r_o is the rotating cylinder radius (rotor), g is the radial airgap clearance, and υ is the kinematic viscosity of the air.

Eq. (5) expresses the Taylor number in its square root form, in which the group is written as the product of the rotational Reynolds number and the square root of the curvature ratio. This is the definition adopted by Gazley [38] and by Becker and Kaye [39], and it is the form in general use in the rotating machinery literature. It is related to the Taylor number of the classical linear stability analysis through the following relationship.

$$Ta_{cl} = Ta^2 = \frac{\omega^2 r_o g^3}{\nu^2} \tag{6}$$

The two formulations differ only by a square. The critical value obtained from the classical small-gap stability analysis, and confirmed experimentally by Taylor, is $Ta_{cl} = 1708$, which corresponds to a critical value of $\sqrt{1708} = 41.3$ in the definition of Eq. (5). The threshold of 41.3 quoted in this work and the benchmark value of 1708 are therefore identical statements of the same stability limit, expressed in two different but equally standard non-dimensionalities. The consistency of the two may also be recognised in the piecewise correlation of Eq. (10), in which the transition from the conduction-dominated branch occurs at $Ta = 41$.

It should further be noted that the value of 1708 is derived in the small-gap limit and is a function of the radius ratio, the aspect ratio and the gap width. The present configuration, with a radius ratio of $\eta = 0.96$, an aspect ratio of $\Gamma = 24$ and a gap width of 5.4 mm, lies well within that limit. The geometrical factor defined in Eq. (9) evaluates to $F_g = 0.98$ for this geometry, so that the modified Taylor number of Eq. (8) is within 2% of the Taylor number itself thus no correction to the critical value is required. Where a radial temperature gradient is present, as it is in the diabatic cases considered here, the onset of the vortical regime is shifted slightly relative to the isothermal value; this effect is captured directly by the computational solution, and the value of 41.3 is used in this work only as a reference threshold for identifying the flow regime.

Nusselt number can be calculated for Taylor flow by different correlations. Becker and Kaye [39] created a correlation to calculate the Nusselt number based on the Taylor number as given in Eq. (7).

$$Nu = \begin{cases} 2 & Ta_m < 1700 \\ 0.128 {Ta_m}^{0.367} & 1700 < Ta_m < 10^4 \\ 0.409 {Ta_m}^{0.241} & 10^4 < Ta_m < 10^7 \end{cases} \tag{7}$$

Where Ta_m is the modified Taylor number which can be calculated using Eq. (8).

$$Ta_m = \frac{Ta}{F_g} \tag{8}$$

Where F_g is the geometrical factor that can be calculated using Eq. (9).

$$F_g = \frac{\pi^4 \left[\frac{2r_o - 2.304g}{2r_o - g}\right]}{1697\left[0.0056 + 0.0571\left(\frac{2r_o - 2.304g}{2r_o - g}\right)^2\right]\left[1 - \frac{g}{2r_o}\right]^2} \tag{9}$$

If the airgap size is minimal compared to the rotor radius, then F_g is close to unity and hence Ta_m will be equal to Ta. For that case, Gazley's correlation [38] is used to calculate the Nusselt number based on the Taylor number, as shown in case Eq. (10).

$$Nu = \begin{cases} 1.1 & Ta < 41 \\ 0.117 {Ta}^{0.63} Pr^{0.27} & 41 < Ta < 100 \\ 0.212 {Ta}^{0.5} Pr^{0.27} & 100 < Ta < \infty \end{cases} \tag{10}$$

2.3. Mesh generation and boundary conditions

The CFD software employed for this investigation is ANSYS Fluent 2022R1. The FESS under study comprises three main components: a case, a cylindrical rotor, and an intervening airgap between the case and the rotor. Dimensionless parameters are used to characterise the airgap geometry. The radius ratio, denoted as $\eta = r_o/r_h$, defines the airgap, where r_o and r_h are the radii of the rotor and casing, respectively. The aspect ratio is defined as $\Gamma = L/g$, where L is the rotor length and g is the airgap width, given by $g = r_h - r_o$. In this study, both the rotor radius and length were set to 0.13 m. A radius ratio of 0.96 was selected, resulting in an airgap width of 5.4 mm and a corresponding aspect ratio of 24.

The system incorporates 16 slits, denoted by n. Given that the flow pattern within the FESS allows for the application of periodic conditions, such conditions were imposed on all periodic boundary surfaces [40]. To optimise computational efficiency and resource allocation, the

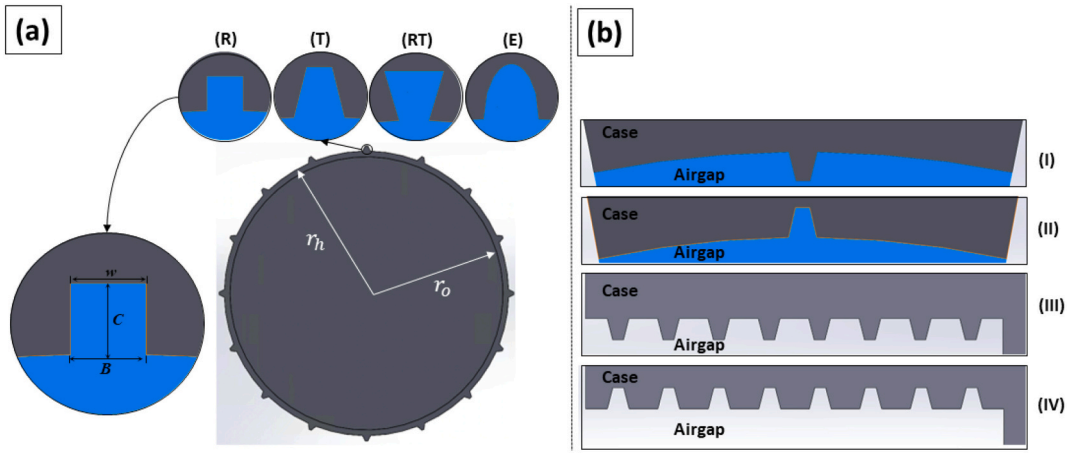


Fig. 2. The geometries for the slit designs, (a) different slit cross sections, (b) different slit orientation and direction.

Table 1
Slit walls geometrical parameters.

Model	Shape	Base length B (mm)	Height C (mm)	Top length w (mm)	B/C
R	Rectangle	2.24	4.47	2.24	0.5
		3.16	3.16	3.16	1
		3.87	2.58	3.87	1.5
T	Trapezoid	2.58	5.16	1.29	0.5
		3.65	3.65	1.83	1
		4.47	2.98	2.24	1.5
RT	Reversed trapezoid	1.83	3.65	3.65	0.5
		2.58	2.58	5.16	1
		3.16	2.11	6.32	1.5
E	Half-ellipse	2.52	5.05	–	0.5
		3.57	3.57	–	1
		4.37	2.91	–	1.5

simulation was conducted on a 22.5° segment of the FESS, incorporating a central symmetry plane. Fig. 1 depicts the baseline FESS geometry devoid of wall slits, serving as a reference within this research context. Fig. 2 illustrates cross-sectional views of the slit walls for four different slit configurations. To ensure a consistent heat transfer area across all models considered, the slit geometry is governed by the parameters specified in Table 1, maintaining a fixed heat transmission area of 10 mm^2.

The hydraulic diameter of a concentric cylinder with slit walls on the out cylinder can be calculated by [20]:

$$D_h = \frac{4 \times \text{Flow Area}}{\text{Wetted Perimeter}} \tag{11}$$

Where the flow area refers to the cross-sectional area through which the fluid passes, and the wetted perimeter denotes the total length of the wall surfaces in direct contact with the fluid.

Optimal mesh quality was achieved by maintaining specific mesh metrics, such as orthogonal quality, in excess of 0.9. Mesh independence analysis is an essential pre-processing step that ensures the accuracy and reliability of numerical simulations. In this study, a structured quadrilateral mesh was applied to model a system in which the rotor and casing mesh dimensions ranged from 2 mm to 5 mm, while the airgap mesh dimension varied between 0.2 mm and 0.5 mm. The primary aim was to determine an optimal mesh configuration for the simulations, achieved by performing a mesh independence study at a maximum rotational speed of 2400 rad/s. The skin friction coefficient and the Nusselt number were the key parameters monitored throughout this assessment.

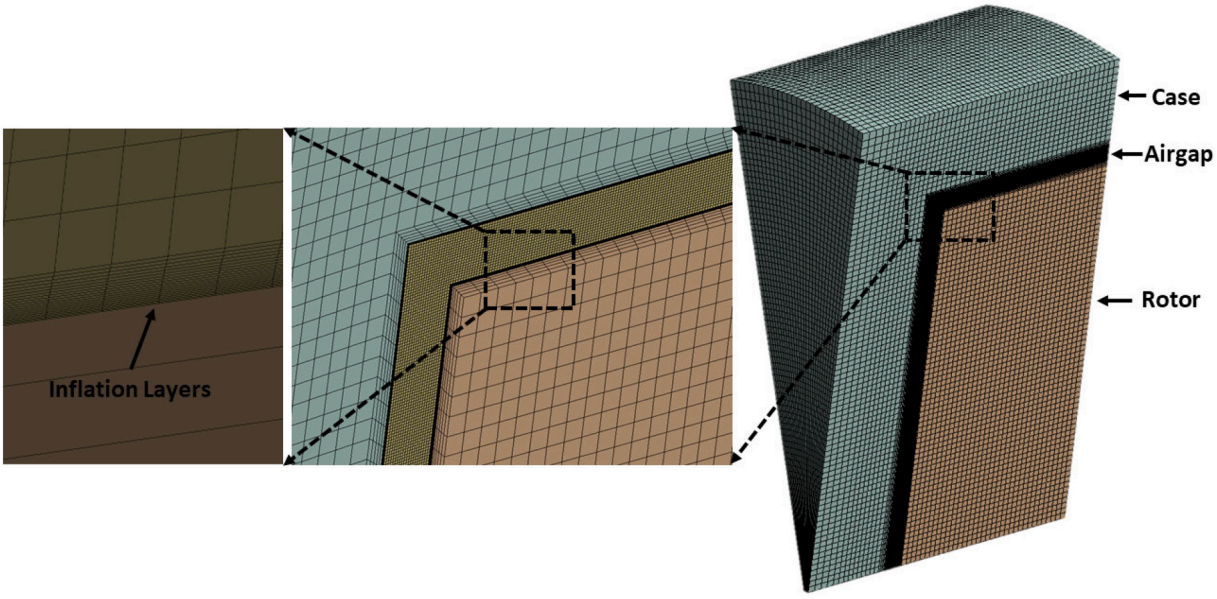


Fig. 3. The quadrilateral mesh used to model the FESS.

Table 2
Summary of the numerical settings.

Item	Setting
Solver	ANSYS Fluent 2022 R1, pressure-based, steady state
Rotational treatment	Moving reference frame (MRF)
Turbulence model	SST k–ω
Pressure–velocity coupling	Coupled
Gradient discretisation	Least-squares cell-based
Pressure discretisation	Second order
Momentum, energy and turbulence discretisation	Second-order upwind
Working fluid	Air as an ideal gas; viscosity from Sutherland's law
Flywheel radius	0.13 m
Internal pressure	0.2, 0.6, 1.0 bar
Rotational velocity	1200, 1600, 2400 rad/s
Tangential speed at flywheel outer edge	156, 234, 312 m/s
Initial and ambient temperature	24 °C (297.15 K)
External casing surface	24 °C (297.15 K)
Rotor surface and casing bore	No-slip walls, coupled thermal condition
Near-wall resolution	$y^+ \leq 1$
Convergence criteria	Scaled residuals $<10^{-6}$; monitored rotor temperature, casing heat flux and rotor wall shear stress constant to within 0.1% over the iterations

Table 3
Verification of the periodic boundary condition.

Computational domain	Deviation in C_w (%)	Deviation in C_m (%)	Deviation in total windage loss (%)	Deviation in rotor surface temperature (%)
Full 360° annulus	reference	reference	reference	reference
90° periodic sector	−0.11	−1.68	+2.12	−2.41
22.5° periodic sector	+1.04	−0.44	+1.37	−0.55

Multiple cases were scrutinised to validate the robustness of the findings, inclusive of the most intricate mesh configurations incorporating slit walls for each geometrical shape investigated, such as the foundational model.

The total number of mesh elements investigated ranged from 1.5 million to 20 million. Based on the outcomes of the mesh independence tests, a mesh configuration consisting of 14 million elements was selected, as it provided an appropriate balance between computational efficiency and solution accuracy. In numerical investigations, careful selection of both mesh type and quality is critical to obtaining reliable results. Fig. 3 illustrates the optimal mesh configuration adopted for this study.

To investigate the steady-state behaviour of the system, a three-dimensional steady-state turbulent flow model was adopted. The time-averaged steady-state solutions accounting for relative rotational motion were obtained using the Moving Reference Frame (MRF) approach. Within this framework, the rotor walls were assigned as rotating moving walls, while all remaining system components were treated as stationary walls. This methodology is well suited to steady-state analyses and is capable of resolving a wide range of flow parameters, including mass flow rates and pressure gradients across rotating components [41].

Since the Reynolds number within the airgap corresponded to the turbulent regime across all rotational speeds examined, the use of a turbulence model was necessary. Drawing on a review of the literature on turbulence modelling for Taylor-Couette flow in concentric cylinder arrangements, applicable to narrow-gap annuli with high-swirl rotational flow, the Reynolds-averaged Navier-Stokes (RANS) equations were solved using the Shear-Stress Transport (SST) K-ω turbulence model. This model has been demonstrated to be effective in predicting fluid flow and heat transfer characteristics in concentric cylinder geometries [42–45].

The viscosity of air, modelled as an ideal gas, was determined using

Table 4
The continuous factors and their levels.

Parameters	Levels		
	Lower level (−1)	Intermediate level (0)	Higher level (+1)
A: Base Length-to-Height Ratio (B/C)	0.5	1	1.5
B: Rotational velocity (rad/s)	1200	1800	2400
C: Pressure (bar)	0.2	0.6	1

Table 5
The categorical factors and their levels.

Parameters	Levels			
D: Modification direction	Radial	Axial		
E: Modification configuration	Grooved inside the case	Inserted to the case		
F: Modification shape	Rectangle (R)	Trapezoid (T)	Reversed trapezoid (RT)	Half-ellipse (E)

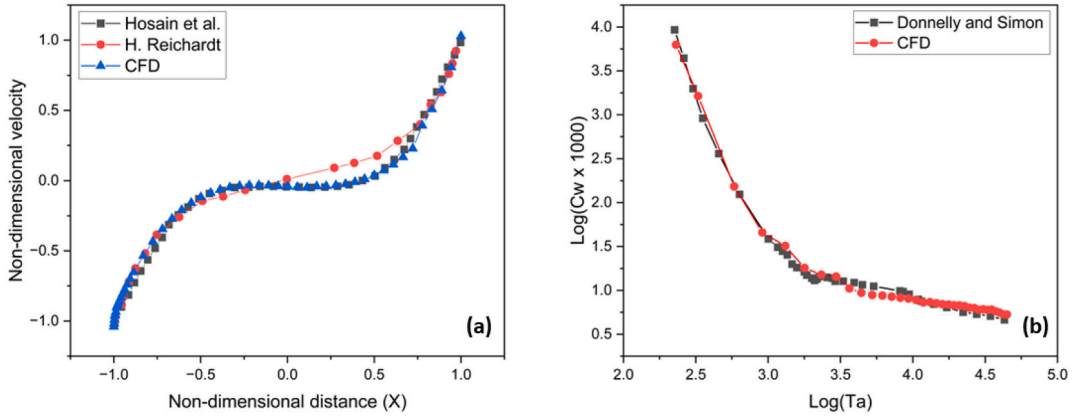


Fig. 4. The validation for (a) the average velocity profile between CFD and experimental data, (b) the skin friction coefficient of the rotor concerning Taylor number.

Table 6
Analysis of variance for windage losses.

Source	Sum of Squares	df	Mean Square	F-value	*p*-value
Model	138.71	42	3.30	3304.46	< 0.0001
A-B/C	0.0169	1	0.0169	16.95	< 0.0001
B-Rotational Velocity	90.20	1	90.20	90,251.21	< 0.0001
C-Pressure	34.11	1	34.11	34,126.84	< 0.0001
D-Direction	3.46	1	3.46	3463.11	< 0.0001
E-Design	4.76	1	4.76	4764.50	< 0.0001
F-Shape	0.1309	3	0.0436	43.67	< 0.0001
AD	0.0380	1	0.0380	38.06	< 0.0001
AE	0.0533	1	0.0533	53.31	< 0.0001
AF	0.0113	3	0.0038	3.77	0.0116
BC	0.0515	1	0.0515	51.50	< 0.0001
BD	0.0239	1	0.0239	23.88	< 0.0001
BE	0.0239	1	0.0239	23.87	< 0.0001
CD	0.0212	1	0.0212	21.16	< 0.0001
DE	2.11	1	2.11	2115.57	< 0.0001
DF	0.0127	3	0.0042	4.22	0.0064
EF	0.0327	3	0.0109	10.91	< 0.0001
A^2	0.0113	1	0.0113	11.30	0.0009
B^2	1.74	1	1.74	1736.28	< 0.0001
C^2	1.94	1	1.94	1937.36	< 0.0001
Residual	0.1969	197	0.0010		
Total	138.90	239			

Table 7
Analysis of variance for Nusselt number.

Source	Sum of Squares	df	Mean Square	F-value	p-value
Model	6.28	72	0.0872	335.27	< 0.0001
A-B/C	0.0524	1	0.0524	201.56	< 0.0001
B-Rotational Velocity	0.3224	1	0.3224	1240.02	< 0.0001
C-Pressure	4.25	1	4.25	16,345.26	< 0.0001
D-Direction	0.0047	1	0.0047	18.11	< 0.0001
E-Design	0.2312	1	0.2312	889.28	< 0.0001
F-Shape	0.0986	3	0.0329	126.37	< 0.0001
AC	0.0008	1	0.0008	3.16	0.0772
AD	0.0013	1	0.0013	4.86	0.0288
AE	0.0015	1	0.0015	5.60	0.0191
AF	0.0204	3	0.0068	26.20	< 0.0001
BC	0.1900	1	0.1900	730.84	< 0.0001
BD	0.0339	1	0.0339	130.25	< 0.0001
BE	0.0543	1	0.0543	209.00	< 0.0001
BF	0.0026	3	0.0009	3.29	0.0222
CD	0.0177	1	0.0177	67.96	< 0.0001
CE	0.0320	1	0.0320	123.19	< 0.0001
DE	0.4278	1	0.4278	1645.77	< 0.0001
DF	0.0287	3	0.0096	36.85	< 0.0001
EF	0.0159	3	0.0053	20.43	< 0.0001
A^2	0.0020	1	0.0020	7.60	0.0065
B^2	0.1283	1	0.1283	493.48	< 0.0001
C^2	0.2856	1	0.2856	1098.73	< 0.0001
Residual	0.0434	167	0.0003		
Total	6.32	239			

Table 8
The fit statistics for the obtained initial response.

First Response	**Std. Dev.**	0.0316	**R^2**	0.9986
	Mean	6.63	**Adjusted R^2**	0.9983
	C.V. %	0.4771	**Predicted R^2**	0.9979
			Adequate Precision	247.264
Second Response	**Std. Dev.**	0.0161	**R^2**	0.9931
	Mean	1.58	**Adjusted R^2**	0.9902
	C.V. %	1.02	**Predicted R^2**	0.9833
			Adequate Precision	75.255

Sutherland's law. The boundary conditions for the computational solution were defined by the absence of any system inlets or outlets. The initial temperature of all system components was set to 24 °C. To accurately capture the flow profiles within the wall boundary layers, wall treatment models were incorporated, and a high-resolution boundary layer mesh was constructed using the wall cell $y_+ \leq 1$ parameter to resolve the viscous sublayer with sufficient precision.

All simulations were advanced to a steady state, and every temperature reported in this work is taken from the converged steady-state field. The energy equation was solved simultaneously with the continuity and momentum equations, with the viscous dissipation term retained, so that the frictional work performed by the rotor on the enclosed air constitutes the only heat source within the domain. The external surface of the casing was assigned the ambient temperature of 24 °C, representing a housing exposed to the surrounding environment, while the rotor surface and the casing bore were treated as no-slip walls with coupled thermal conditions. The steady state therefore corresponds to the condition in which the heat generated by viscous dissipation within the airgap is balanced by the heat conducted through the casing to the ambient boundary; under this balance the rotor surface, the enclosed air and the casing bore each attain a distinct and constant temperature, and it is the difference between these temperatures that enter the definition of the Nusselt number given below.

The correlations of Eqs. (7) and (10) are employed in this work as a reference for the airgap Nusselt number of a smooth annulus; the heat transfer response used in the optimisation is extracted directly from the converged solution and is defined as follows. Three area-averaged convective heat transfer coefficients are obtained from the computation: $h_{r,c}$ on the cylindrical lateral surface of the rotor, $h_{r,e}$ on the two rotor end faces, and h_h on the casing bore, each referred to the difference between the corresponding wall temperature and the volume-averaged temperature of the air in the adjacent gap. These are combined into a single Nusselt number obtained through the following expression.

$$Nu = \frac{h_{r,c}\, g_e + h_{r,e}\, g_s}{2\lambda} + \frac{h_h\, g_e}{\lambda} \tag{12}$$

where g_e is the equivalent airgap width of the slit annulus, taken as one half of the hydraulic diameter given by Eq. (11), g_s is the axial clearance between the rotor end faces and the casing end walls, and λ is the thermal conductivity of air evaluated at the mean temperature of the enclosed air. The first term of Eq. (12) is the arithmetic mean of the two rotor-side Nusselt numbers and measures the transfer of the dissipated heat from the rotor into the enclosed air; the second term is the casing-side Nusselt number and measures the transfer of that heat from the air into the casing.

The use of an equivalent airgap width in place of the geometric airgap width is necessary because the slits alter both the flow area and the wetted perimeter of the annulus. For a smooth annulus the hydraulic diameter of Eq. (11) reduces exactly to twice the airgap width, so that $g_e = g$ and the definition is continuous with that of the baseline with no slit. For the geometries examined here g_e lies between 4.79 mm and 5.38 mm, against a geometric airgap width of 5.40 mm, the smaller values corresponding to the inserted configurations in which the slit intrudes into the annulus. All quantities in Eq. (12) are taken from the steady-state solution, and the definition is applied to the smooth baseline and to every slit configuration.

Convergence was assessed both from the scaled residuals of the governing equations and from the behaviour of monitored integral quantities. The solution was considered converged when the scaled residuals of the continuity, momentum, energy and turbulence equations had fallen below 10^{-6} and when the area-averaged rotor surface temperature, the area-averaged heat flux through the casing bore and the area-averaged wall shear stress on the rotor had each ceased to vary by more than 0.1% over the successive iterations. The principal numerical settings are summarised in Table 2.

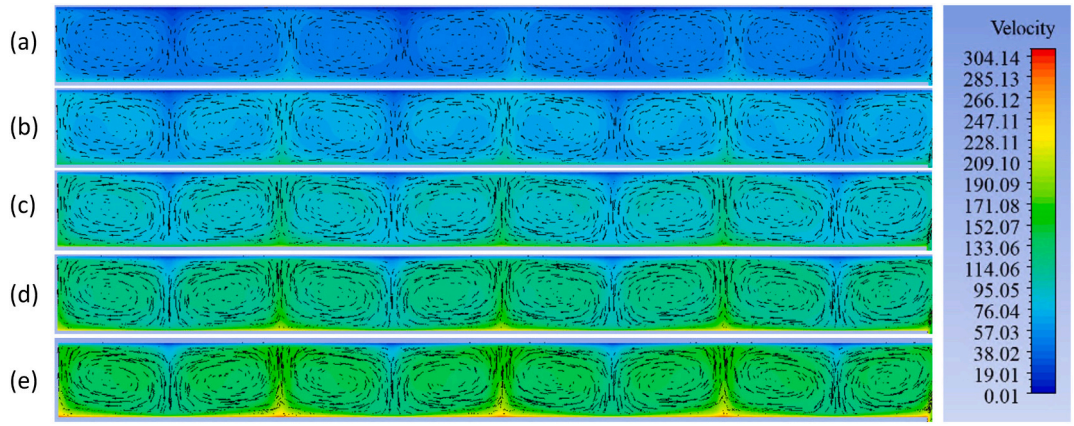


Fig. 5. Velocity contour of the FESS with no slits under 1 bar pressure at the rotational velocity of (a) 800 rad/s, (b) 1200 rad/s, (c) 1600 rad/s, (d) 2000 rad/s, and (e)2400 rad/s.

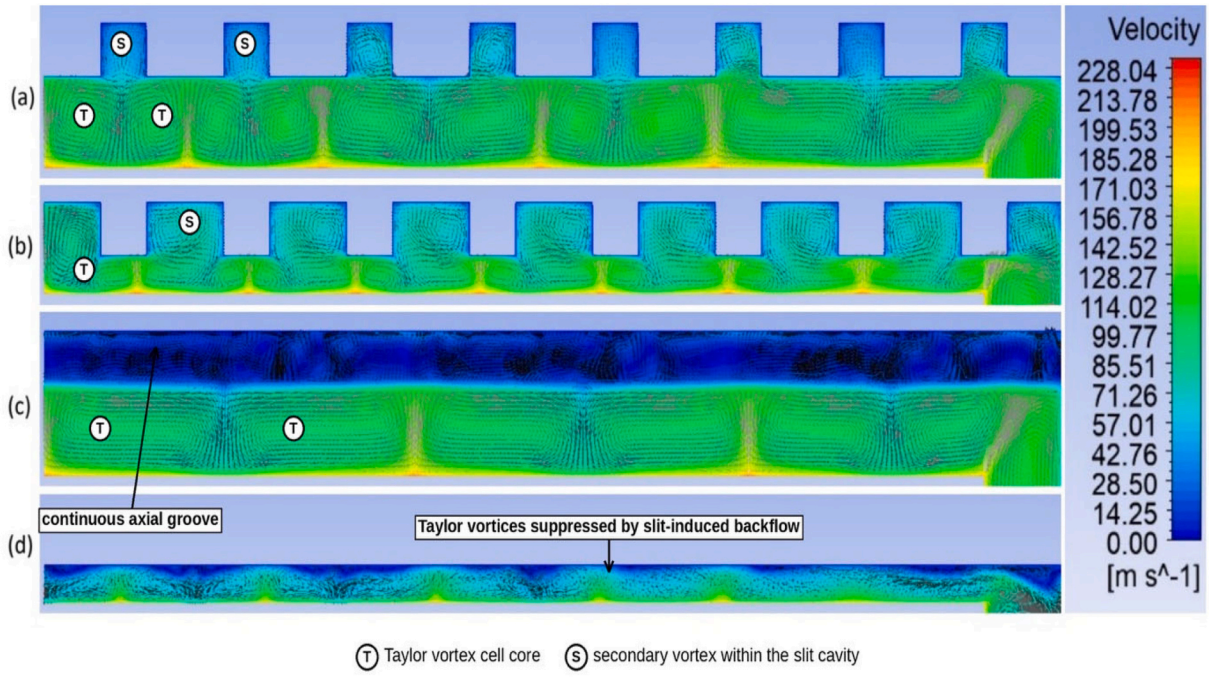


Fig. 6. Velocity contour of the FESS in Y-Z plane for rectangle shape under 1 bar pressure and rotational velocity of 1600 rad/s as a function of factors D and E where: (a) radial/grooved, (b) radial/inserted, (c) axial/grooved, and (d) axial/inserted.

2.4. Verification of the periodic boundary condition

The reduction of the computational domain to a single 22.5° sector rests on the assumption that both the flow field and the temperature field are rotationally periodic with the angular pitch of the slit array. The slits are equally spaced and geometrically identical in every configuration considered, so that the casing bore is invariant under rotation through $360°/n = 22.5°$; the configurations examined here contain no azimuthal asymmetry in the slit spacing, dimension or orientation, and the sector therefore constitutes a true unit cell of the geometry. No azimuthal variation is imposed on any thermal boundary: the external casing temperature is uniform, the rotor is axisymmetric and rotates about its own axis, and the only heat source in the domain is the viscous dissipation generated within the airgap, which is distributed with the periodicity of the geometry. The temperature field inherits the periodicity of the boundary conditions, and the sector reduction remains valid in the conjugate, heat-transfer-involved case. Rotational periodicity is applied on the two sector faces, so that the azimuthal transport of momentum and enthalpy across those faces is retained in full and the swirling flow is not artificially constrained.

Because the underlying flow is turbulent, and the Taylor vortices are not individually constrained to the sector pitch, the validity of the periodicity assumption was verified numerically. Three models of the smooth-wall configuration were constructed and solved under identical conditions at a rotational velocity of 2400 rad/s and ambient pressure: the complete 360° annulus, a 90° rotationally periodic sector, and the 22.5° sector adopted for the production simulations. The comparison is presented in Table 3. The total windage loss predicted on the 22.5° sector differs from that of the full annulus by 1.4%, and the corresponding rotor surface temperature by 0.6%; for the 90° sector the deviations are 2.1% and 2.4%, respectively. The two components of the windage loss are reproduced individually to within 1.1% for the cylindrical skin friction coefficient and 0.5% for the disc torque coefficient. These deviations are an order of magnitude smaller than the differences between the slit configurations that the parametric study is intended to resolve and are of the same order as the iterative convergence tolerance

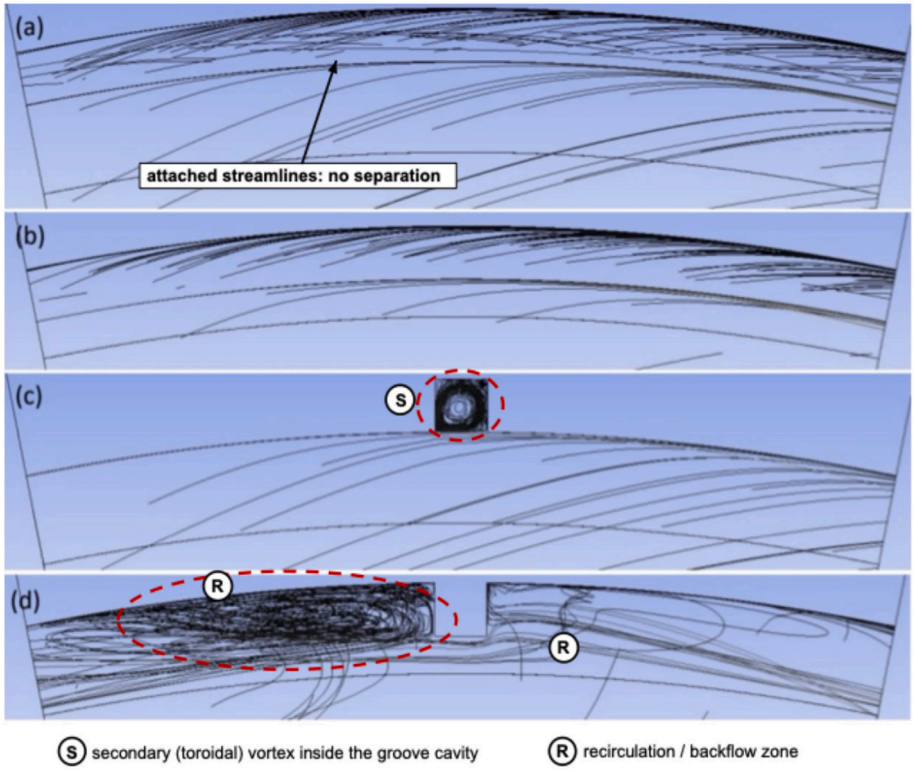


Fig. 7. The streamlines distribution of the FESS in X-Y plane for rectangle shape under 1 bar pressure and rotational velocity of 1600 rad/s as a function of factors D and E where: (a) radial/grooved, (b) radial/inserted, (c) axial/grooved, and (d) axial/inserted.

of the solution.

2.5. Numerical model validation

Fig. 4a presents the predicted mean velocity profile in comparison with experimental data obtained from previous studies by Hosain et al. [46] and H. Reichardt [47]. To enable a fair comparison, the simulated velocity values were normalised to align with the range of the experimental data. In Fig. 4a, the non-dimensional coordinates correspond to the casing wall and the rotor wall, respectively. At low Reynolds numbers, the velocity profile displays a linear trend, whereas at higher Reynolds numbers, a steep gradient develops near the walls as a result of viscous forces in the near-wall region. The midpoint of the airgap is identified as the location of the mean velocity. The computed mean velocity profile shows good agreement with experimentally measured profiles, and consistent trends have been reported in earlier studies [48,49].

The variation of the skin friction coefficient with the Taylor number was assessed against experimental data reported by Donnelly [50], with the radius ratio matching that of the CFD model. Fig. 4b illustrates the distributions of the skin friction coefficient and Taylor number, identifying three distinct flow regimes. The first corresponds to laminar flow without vortices, the second to laminar flow with developing Taylor-Couette vortices, referred to as being consistent with non-linear theory due to the non-linear variation of the skin friction coefficient, and the third to turbulent flow characterised by uniformly mixed enclosed air. The numerically obtained critical Taylor numbers show close agreement with values reported in the literature. Furthermore, where Taylor vortices are present within the airgap, the skin friction coefficients predicted by the CFD model are consistent with the experimental results of Donnelly [50].

Experimental findings from the authors have additionally contributed to the validation of the CFD model [5]. Both experimental and numerical results are in good agreement, demonstrating comparable flow behaviour, with discrepancies between the two datasets remaining within a 15% margin.

3. Response surface methodology (RSM)

RSM is a statistical approach designed to analyse multifactorial studies using a reduced number of experimental or computational trials. It is particularly well suited to complex problems in which multiple independent variables simultaneously influence a dependent response. Box-Behnken designs play an important role in this context, producing higher-order response surfaces with fewer runs than conventional factorial approaches. The Box-Behnken design comprises a specific arrangement of twelve intermediate edge nodes and three central nodes, configured to fit a quadratic model. This design strategically positions points at the midpoints of the edges of the cubic design space, together with central points, to enhance the statistical robustness of the analysis [27].

RSM represents an accurate and computationally efficient framework for designing simulations, analysing results, and optimising system performance in the context of FESS parameter studies. Its application is particularly valuable for developing a comprehensive understanding of how slit wall geometry affects the formation and intensity of vortices within the slit regions, as well as the consequent effects on flow field distribution, heat transfer, and windage losses. RSM therefore plays a critical role in identifying optimal operating parameters, contributing to improved efficiency and reliability in energy system outputs, and underscoring its broader significance in fluid dynamics and energy system optimisation.

3.1. Responses selection

The system responses are selected to characterise the local form of the response surface by capturing the interactions and individual effects of the system parameters. They are also employed to assess the system's

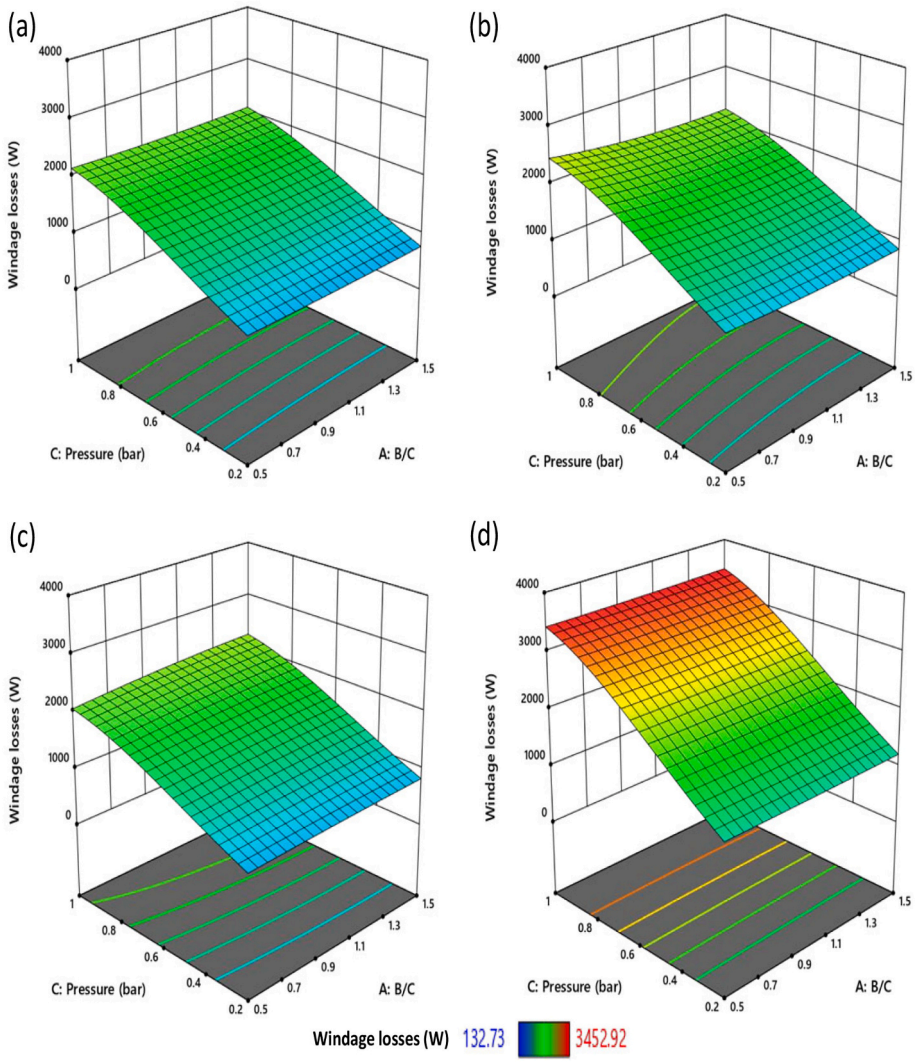


Fig. 8. 3D plot of windage losses for a rectangle shape as a function of factors D and E where: (a) radial/grooved, (b) radial/inserted, (c) axial/grooved, and (d) axial/inserted.

performance capabilities and limitations, as well as to identify optimal system configurations. This study examines two responses: windage loss and the Nusselt number. The Nusselt number is a key metric for quantifying convective heat transfer within the airgap and assessing its sensitivity to variations in design parameters. An increase in the Nusselt number enhances convection-driven heat transfer, offering the dual advantage of reducing rotor temperature and decreasing dependence on internal cooling mechanisms. This improved thermal management permits higher rotational speeds, potentially increasing the kinetic energy storage capacity of the system. Simultaneously, windage loss serves as a key indicator of frictional losses within a FESS, directly affecting the system's self-discharge rate. By analysing these two parameters, this study seeks to optimise the operational efficiency and energy conservation performance of the FESS, while identifying priority areas for future research and development in energy storage technologies.

3.2. Factors selection

The incorporation of slit walls into the FESS casing is a novel aspect of this study. The slits, which have a variety of cross-sectional geometries such as rectangle, trapezoid, reversed trapezoid, and half-ellipse, are intended to improve system efficiency. The primary goal is to strategically change the internal architecture of the casing to reduce windage losses and increase heat transfer rate. The slit wall area is consistently maintained throughout the designs, providing a consistent variable for accurate comparative analysis. This study examines a wide range of parameters to thoroughly assess their influence on FESS performance. The factors considered include the rotor rotational velocity, internal pressure, slit wall geometry, the base length-to-height ratio (B/C) of the slits, slit direction, and slit wall configuration. The rotor rotational velocity is fixed at 2400 rad/s, representing the maximum allowable speed for a solid steel cylindrical rotor at a safety factor of two [51].

Table 4 presents the continuous factors along with their respective levels, expressed in both actual and coded values. The upper and lower bounds of the factors are encoded as +1 and − 1, respectively, with 0 denoting the intermediate level [27]. The categorical factors used in the analysis are presented in Table 5 and illustrated in Fig. 2. This study examines the flow field distribution, windage losses, and heat transfer characteristics of turbulent flow within a FESS. To the best of the authors' knowledge, this represents the first investigation into the effect of casing slit geometries on windage loss reduction in a flywheel energy storage system.

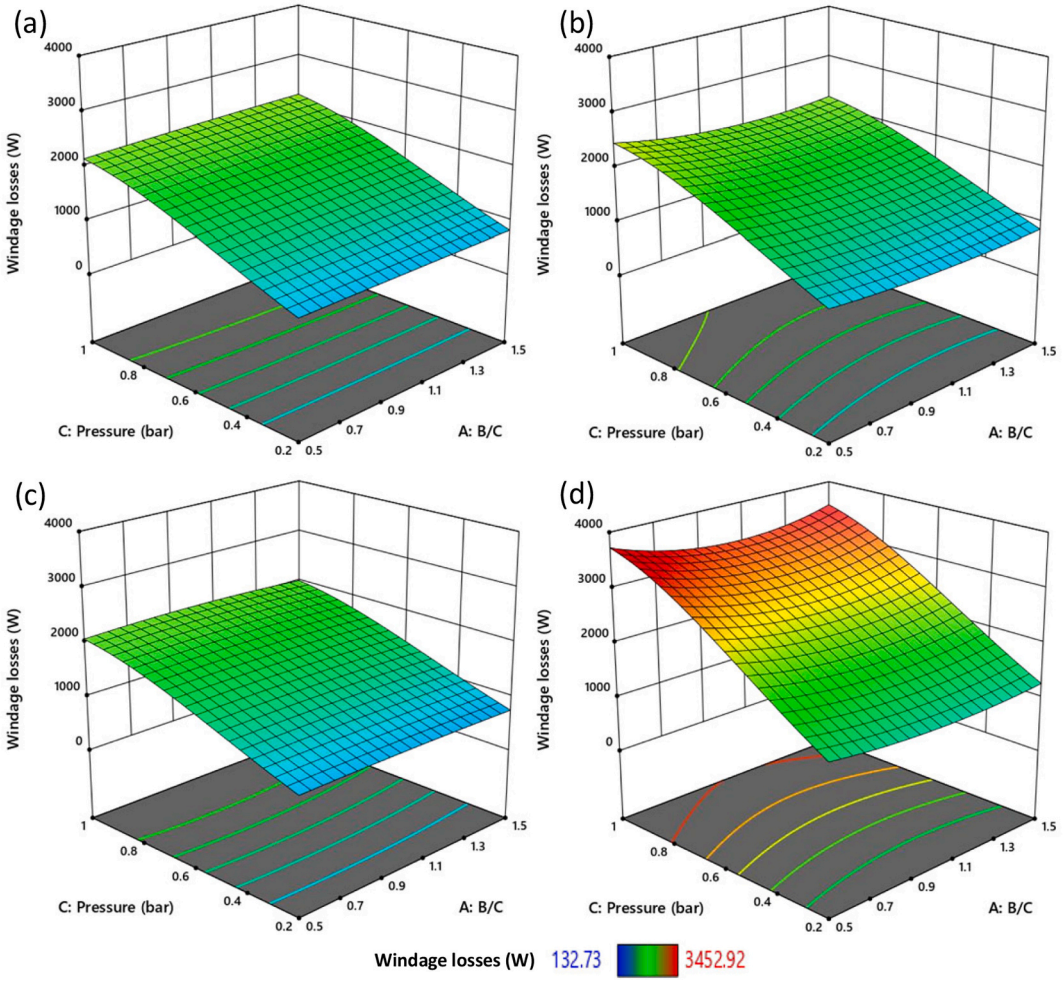


Fig. 9. 3D plot of windage losses for a trapezoid shape as a function of factors D and E where: (a) radial/grooved, (b) radial/inserted, (c) axial/grooved, and (d) axial/inserted.

4. Results and discussion

4.1. Response

Windage loss and the Nusselt number were subjected to a comprehensive analysis of variance (ANOVA). Tables 6 and 7 present the results for windage loss and the Nusselt number, respectively, identifying the significant factors and their interactions. Both models were found to be statistically significant, as indicated by F-values of 3304.46 and 335.27 for windage loss and the Nusselt number, respectively. Model terms with *P*-values below 0.05 were considered statistically significant, while those with *P*-values exceeding 0.10 were deemed insignificant. As shown in Tables 6 and 7, certain responses were identified as significant, leading to the removal of insignificant terms to enhance the predictive accuracy of the models. The F-values for individual factors and their interactions were computed to assess the significance of their mean square variations, while the corresponding *P*-values were determined using a 95% confidence interval. The statistical outcomes confirm the capability of both models to predict windage losses and Nusselt numbers within the range of the numerical variables examined.

4.2. Model adequacy

In regression analysis, the mathematical model is used to describe the relationship between the input variables and the dependent responses. The fit statistics for the preliminary response, presented in Table 8, demonstrate a strong coefficient of determination (R^2) exceeding 0.98, indicating a close agreement between the regression model and the actual response data points. The adjusted R^2 values, refined by removing non-contributing parameters, also remain above 0.98, reflecting minimal variability in the data. The predictive capability of the model for new observations is assessed through the predicted R^2 value. A difference of no greater than 0.2 between the predicted and adjusted R^2 values indicates a satisfactory level of model correlation.

4.3. Fluid flow characteristics

As the rotational velocity of a FESS increases, the Taylor-Couette vortices that develop within the airgap become increasingly pronounced. These vortices originate from the relative motion between the inner and outer cylinders of the system, and their formation is governed by several factors, including airgap dimensions, rotational velocity, and the fluid properties within the airgap. At low rotational velocities, the Taylor-Couette vortices tend to be relatively weak and less defined; however, as the rotational velocity increases, the vortices grow in intensity and transition towards a more turbulent state, as illustrated in Fig. 5. This progression has several consequences for overall FESS performance, including elevated windage losses and a reduction in the heat transfer rate. One of the primary mechanisms through which slit walls influence the Taylor-Couette vortices is by disrupting the flow within the airgap. The introduction of these geometric features compels the fluid to navigate around the slit wall profile, thereby modifying the flow pattern

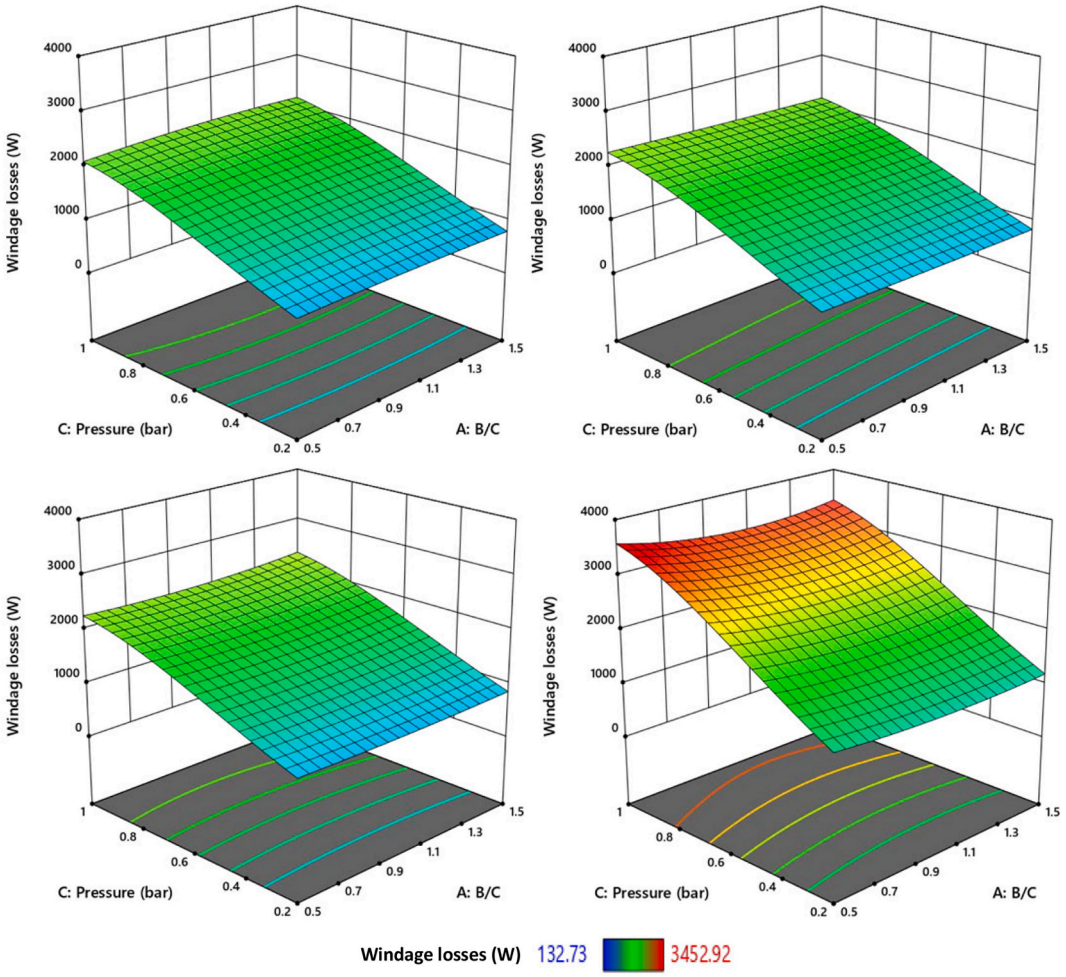


Fig. 10. 3D plot of windage losses for a reversed trapezoid shape as a function of factors D and E where: (a) radial/grooved, (b) radial/inserted, (c) axial/grooved, and (d) axial/inserted.

and altering the intensity of the vortices, as shown in Fig. 6.

As fluid flows through the annular gap, interactions with the bounding walls are initiated by the combined influence of inertial forces and boundary layer separation, leading to the development of complex vortex structures. The shape and organisation of these vortices are governed by parameters D and E. A key factor influencing the occurrence of Taylor vortices is the airgap width between the concentric cylinders. A reduced airgap is associated with an increase in the number of Taylor vortices, which in turn exerts a significant effect on the skin friction coefficient, resulting in elevated windage losses. Taylor vortices occur more frequently as the airgap widens, whereas Taylor cells are less readily affected by azimuthal waves as the airgap narrows [52]. It is important to note that, although the airgap dimension remains consistent across all configurations examined, those featuring inserted slits, as opposed to grooved ones, effectively present a narrower airgap, thereby promoting a higher occurrence of Taylor vortices. Among the configurations investigated, the axial/grooved arrangement produces the fewest Taylor vortices, whereas the radial/inserted configuration generates the greatest number, as illustrated in Fig. 6.

In the axial-inserted configuration, although the number of Taylor cells is not at its highest, the slit disrupts the smooth passage of air through the gap. This deflection directs a portion of the air particles towards the rotor, resulting in a considerable increase in the skin friction coefficient, as shown in Fig. 7. For the axial direction, a deviation in the velocity streamlines is observed relative to the more direct radial direction. When the slit is grooved, air is channelled into the slit cavity, generating minor toroidal vortices that have a limited effect on redirecting air particles towards the rotor. In contrast, an inserted slit produces a pronounced backflow effect, whereby the velocity streamlines are deflected upon encountering the slit and a portion of the flow is redirected towards the rotor. This mechanism contributes to an increase in the skin friction coefficient.

4.4. Windage loss response

Windage losses result from the viscous friction between the rotor surface and the surrounding fluid during flywheel rotation. Parameters such as rotational speed and the thermophysical properties of the enclosed fluid play a significant role in determining the magnitude of these losses. An analysis was performed to evaluate the effect of rotational speed on windage losses across the various configurations examined. As rotational speed increases, the air velocity distribution within the airgap is altered, attributed to the Taylor number exceeding its critical threshold of 41.3, which triggers the formation of Taylor vortices.

Fig. 8 provides a detailed representation of windage losses for the rectangular slit shape, highlighting the interaction between the base length-to-height ratio (B/C) and the cavity pressure. A consistent reduction in windage losses is observed with decreasing pressure, regardless of the slit direction or configuration. Moreover, an increase in the B/C ratio leads to a notable reduction in windage losses, a trend that is particularly pronounced in the inserted configuration compared to the grooved one, as demonstrated in Fig. 8(b) and 8(d). However, the effect of an increasing B/C ratio is less significant in the grooved configuration.

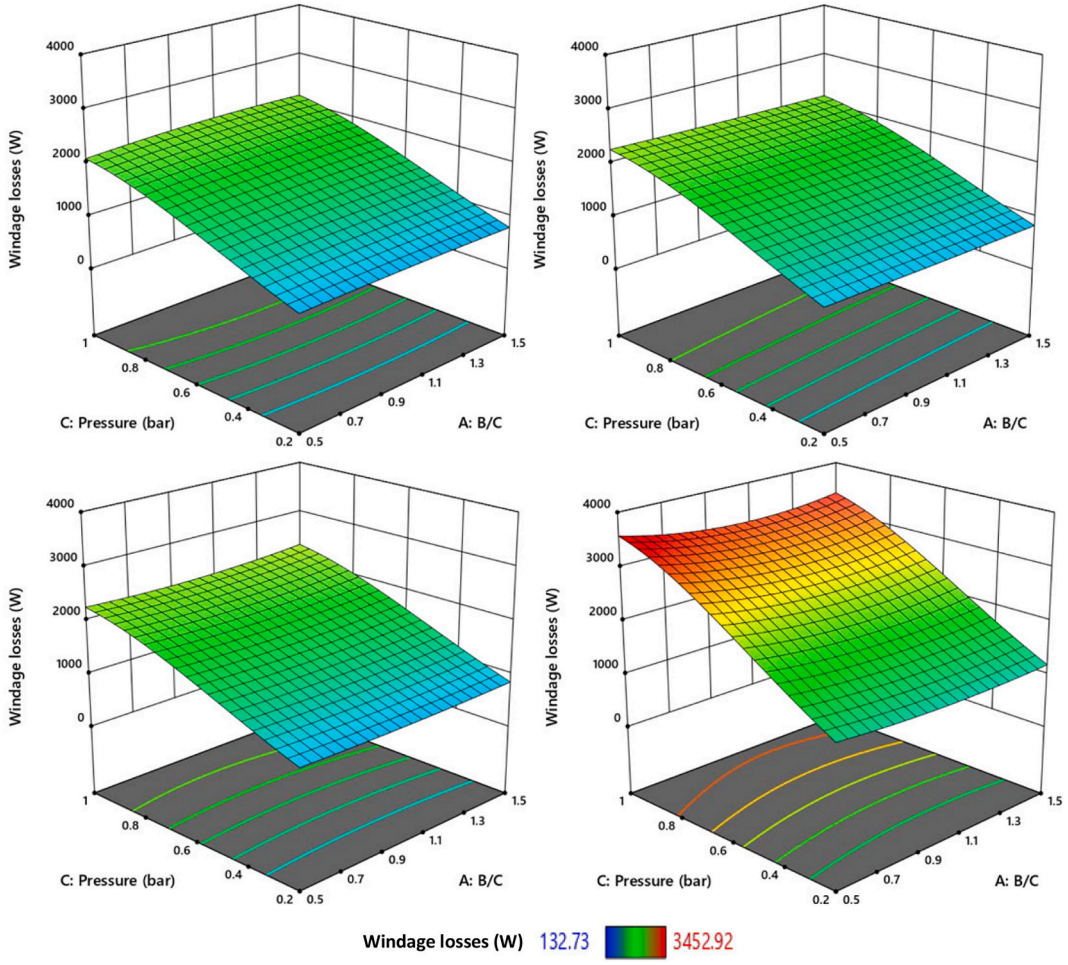


Fig. 11. 3D plot of windage losses for a half-ellipse shape as a function of factors D and E where: (a) radial/grooved, (b) radial/inserted, (c) axial/grooved, and (d) axial/inserted.

The minimum windage losses were associated with the axial direction combined with the grooved configuration, while the maximum windage losses corresponded to the axial direction paired with the inserted configuration.

In the radial direction, the airflow aligns with the Taylor vortices, producing a reduced skin friction coefficient, since the number of Taylor vortices constitutes the dominant contributing factor. This leads to a lower rotor temperature and consequently reduced windage losses. In contrast, the grooved configuration promotes enhanced heat transfer, maintaining a lower rotor temperature compared to the inserted configuration. The inserted arrangement adversely affects the skin friction coefficient, primarily due to the amplification of Taylor vortices associated with this configuration. This amplification is driven by the reduction in the airgap adjacent to the rotor; as the airgap decreases, the number of Taylor vortices increases correspondingly. It is also notable that the dimensions of the Taylor cells closely correspond to the width of the airgap.

For the trapezoid slit shape, Fig. 9 illustrates the windage losses and clarifies the relationship between the B/C ratio and the cavity pressure. A uniform reduction in windage losses is observed as pressure decreases, owing to the associated reduction in the number of gas particles within the system, a pattern that holds consistently regardless of the slit direction or configuration. Although increasing the B/C ratio contributes to lower windage losses, its influence is comparatively moderate. In particular, for the inserted configuration, the optimal windage loss performance is achieved at a B/C ratio of 1, as shown in Fig. 9(b) and 9 (d). The minimum windage losses were associated with the axial direction combined with a grooved slit design, while the maximum windage losses corresponded to the axial direction paired with an inserted slit configuration.

For the reversed trapezoid slit shape, the effect of the B/C ratio follows a pattern consistent with that observed for the rectangular slit shape. An increase in the B/C ratio produces a significant reduction in windage losses, as shown in Fig. 10, a trend that is particularly evident when an inserted slit design is employed rather than a grooved one. At the maximum pressure level examined, the lowest windage losses were recorded for the radial grooved configuration at a B/C ratio of 1. Conversely, under the same B/C ratio and pressure conditions, the axial inserted configuration yielded the highest windage losses.

Fig. 11 presents the windage losses associated with the half-ellipse slit shape. The data reveals a pattern consistent with the effects of reducing cavity pressure observed in the other configurations. While the influence of increasing the B/C ratio follows a trend similar to that of the trapezoid shape, the minimum windage losses are achieved at a B/C ratio of 1 for the axial direction, whereas in the radial direction, the highest windage losses are recorded at a ratio of 1.5. Across all slit shapes examined, the axial/inserted configuration consistently produces the highest windage losses at all pressures and B/C ratios evaluated. The remaining three configurations, however, yield comparably similar values that are closely grouped together.

The objective of reducing windage losses has been addressed through the systematic analysis of six governing factors. The investigation has shown that matching the base length of a slit to its height represents the optimal slit dimension for effectively minimising aerodynamic drag.

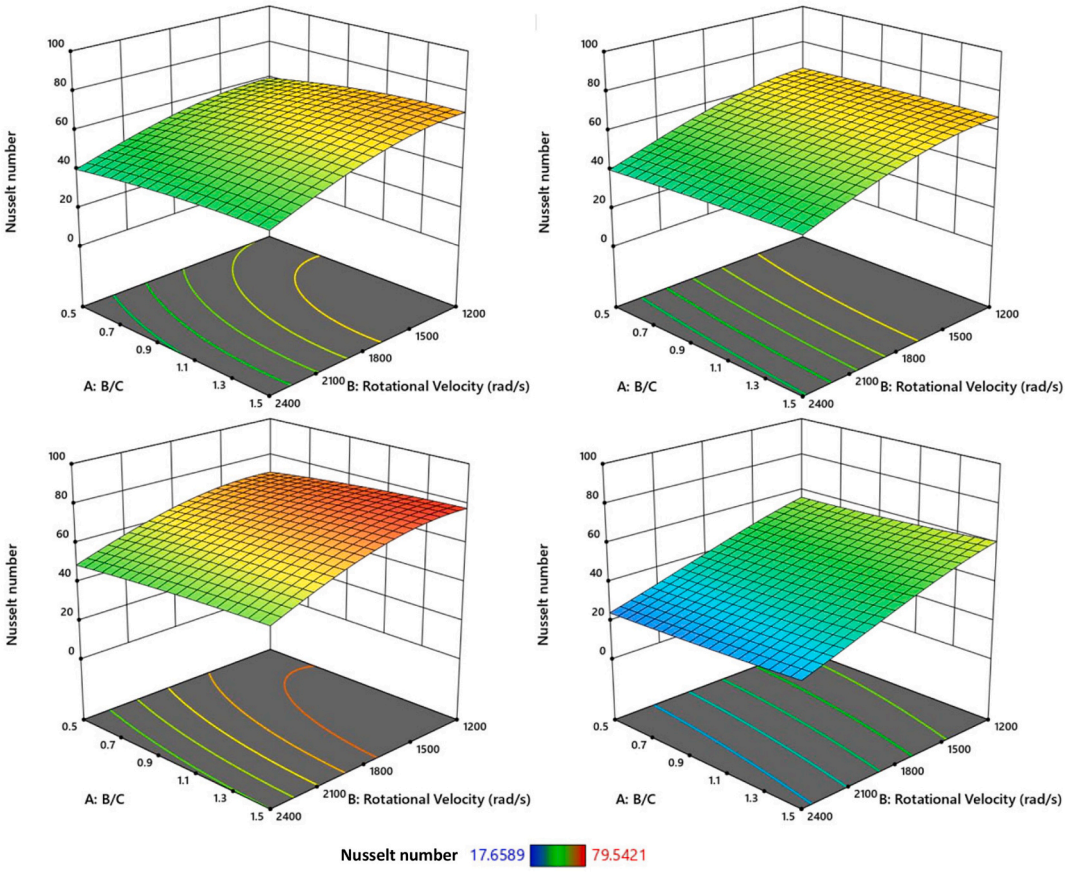


Fig. 12. 3D plot of Nusselt number for a rectangle shape as a function of factors D and E where: (a) radial/grooved, (b) radial/inserted, (c) axial/grooved, and (d) axial/inserted.

Reducing the rotational velocity is equally identified as a critical parameter, as it directly lowers windage losses by decreasing aerodynamic resistance. Minimising the pressure within the cavity also plays an important role, substantially reducing the frictional forces exerted on the rotating components. Orienting the slits in the radial direction is found to align with the natural flow path, thereby reducing turbulence and the associated energy losses. Furthermore, the adoption of a grooved configuration promotes a more streamlined flow and reduced surface friction. Finally, specific slit geometries, such as the reversed trapezoid, are found to be superior in terms of skin friction coefficient reduction, which consequently facilitates a further decrease in windage losses.

4.5. Heat transfer response

The Nusselt number is a key metric for quantifying convective heat transfer between the rotor, the surrounding air, and the flywheel casing. A higher Nusselt number indicates more efficient convection, corresponding to lower temperatures for both the rotor and the casing while remaining within acceptable safety limits. As shown in Figs. 12 to 15, an increase in the B/C ratio is associated with a rise in the Nusselt number across all rotational speeds examined. The highest Nusselt numbers for each slit shape were recorded in the axial grooved configuration, particularly within the rotational speed range of 1200 to 1600 rad/s. A clear relationship between the Nusselt number and the Reynolds number is evident, with the Reynolds number increasing with rotational speed up to 1600 rad/s. Beyond this threshold, the Reynolds number decreases as a consequence of the reduction in the kinematic viscosity of air as the air temperature continues to fall.

Fig. 12 presents the Nusselt number trends for the rectangular slit shape, illustrating the interaction between the B/C ratio and the rotor rotational velocity. An increased B/C ratio enhances the Nusselt number across all configurations within the rectangular slit model, attributed to the wider slit base length, which redirects a greater volume of airflow into the slit cavity. This redirection promotes improved mixing between the hot and cold air streams, driven by the action of Taylor vortices. The Taylor-Couette flow, characterised by a spike-shaped velocity profile within the airgap, is central to this mechanism. In this profile, air velocity is negligible near the casing and reaches its peak in the vicinity of the rotor. Frictional heating between the rotor surface and the adjacent air molecules elevates the temperature of the near-rotor air, which is subsequently transported towards the casing, raising the mixed air temperature. This process is further intensified by centrifugal forces that accelerate the vortices upon collision.

In the axial/inserted configuration, the Nusselt number is considerably lower across all rotational velocities, pressures, and B/C ratios, as a result of flow disruption caused by the redirection of velocity streamlines. This creates a high-pressure zone upstream of the slit and a low-pressure zone downstream, relative to other configurations, as illustrated in Figs. 7 and 15. The backflow induced by the inserted slit modifies the velocity streamlines and generates low-pressure regions that adversely affect heat transfer performance. In contrast, the radial slit direction aligns with the Taylor vortices, and the grooved configuration promotes enhanced heat transfer, yielding lower rotor temperatures and a higher Nusselt number, thereby improving convective heat transfer efficiency. When the slit is grooved, air is drawn into the slit cavity, generating small toroidal vortices that contribute positively to the remixing of hot and cold air streams.

For the trapezoid slit shape, the observed behaviour is consistent with that of the rectangular slit shape, as illustrated in Fig. 13. Within

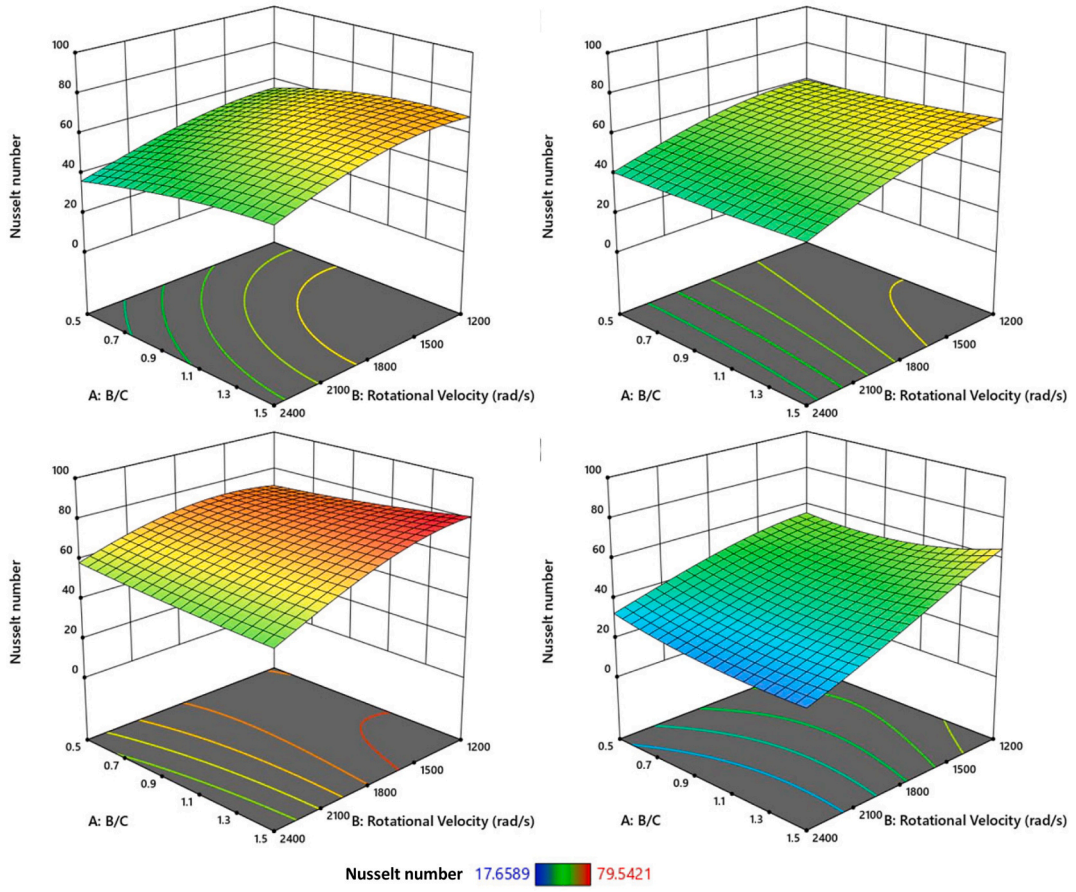


Fig. 13. 3D plot of Nusselt number for a trapezoid shape as a function of factors D and E where: (a) radial/grooved, (b) radial/inserted, (c) axial/grooved, and (d) axial/inserted.

the inserted configuration, the Nusselt number decreases progressively with increasing rotational velocity. In the grooved configuration, however, the Nusselt number remains relatively stable within the rotational velocity range of 1200 to 1600 rad/s. The reversed trapezoid shape, by contrast, exhibits a lower overall Nusselt number compared to both the rectangular and trapezoid shapes. The effect of the B/C ratio on the Nusselt number is also less significant for the reversed trapezoid than for the preceding shapes. Furthermore, an increase in rotational velocity results in a reduction of the Nusselt number across all configurations examined, a trend that is presented in Fig. 14.

An increase in the B/C ratio produces a notable change in the velocity streamlines of the air particles. At the highest B/C ratio examined, the airflow impinges on the slit, redirecting the air particles and generating a high-pressure zone upstream of the slit and a low-pressure zone downstream, as depicted in Fig. 15. At a B/C ratio of 0.5, the airflow remains in close proximity to the rotor surface, a condition that is not favourable for the development of Taylor vortices, as observed in Fig. 16(a). The absence of Taylor vortices is associated with a considerably lower Nusselt number, reflecting minimal thermal mixing between the rotor and the casing in the post-slit region. As the B/C ratio is increased, however, the airflow streamlines are deflected towards the casing at a faster rate, promoting the development of Taylor vortices, as illustrated in Fig. 16. The presence of these inherently oscillatory vortices gives rise to a number of secondary vortices, contributing to a more complex flow pattern and an enhancement of convective heat transfer, as reflected in the variability of the Nusselt number.

The half-ellipse shape demonstrates a higher Nusselt number relative to all other slit shapes evaluated within each specific configuration, as shown in Fig. 17. The influence of the B/C ratio is also most significant for this shape; an increase in the ratio produces a more pronounced amplification of the Nusselt number compared to the other shapes considered. Fig. 18 illustrates that as the fluid passes through the annular gap; it encounters the slit walls. This interaction, driven by inertial forces and boundary layer separation, initiates the formation of small-scale vortex structures. An examination of the streamline patterns across the four models within the slit region reveals that these vortex structures are concentrated within the slit area in all cases. For the half-ellipse shape in particular, a single vortex occupies the entire grooved slit cavity, whereas the remaining shapes exhibit regions identified as flow dead zones. These zones are indicative of reduced heat transfer capability, resulting in considerably lower Nusselt numbers. Flow dead zones are characterised by relatively isolated, low-speed vortices that restrict mass exchange with the main flow within the slit, promoting the formation of a thin boundary layer.

It should be emphasised that the advantage conferred by the absence of dead zones is realised only where the cavity vortex is the controlling heat transfer mechanism, which is the case in the grooved configurations. In the configurations with inserts, the slit protrudes into the annulus, and the governing mechanism changes accordingly. The protrusion reduces the effective radial clearance and acts as an obstruction to the annular flow, generating a separated region and a pronounced backflow that suppress the Taylor vortices responsible for transporting heat from the rotor to the casing, as evident from the streamlines of Fig. 7(d) and from the velocity contours of Fig. 20(d). The reduction in the intensity of the primary vortices is a first-order effect on the Nusselt number, whereas the elimination of the small, low-momentum recirculation within the cavity is a second-order refinement of the mixing that takes place inside the slit. The first effect is by some margin larger,

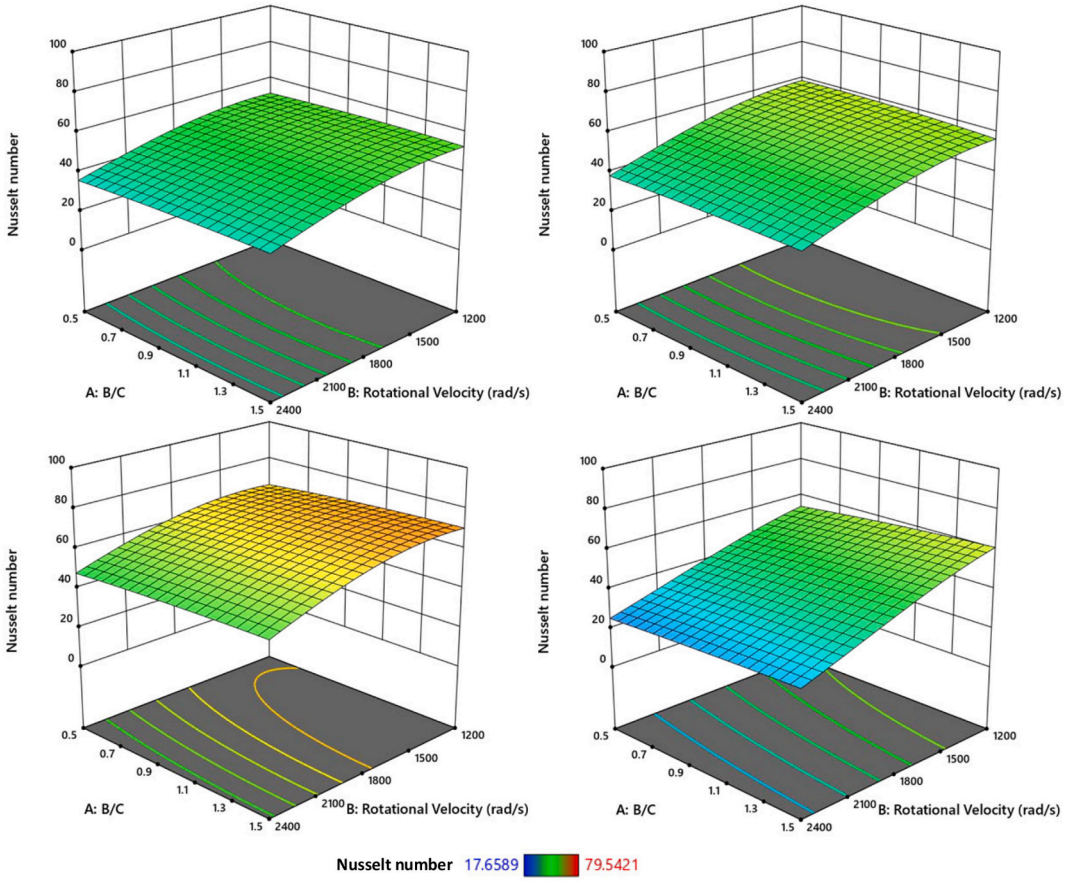


Fig. 14. 3D plot of Nusselt number for a reversed-trapezoid shape as a function of factors D and E where: (a) radial/grooved, (b) radial/inserted, (c) axial/grooved, and (d) axial/inserted.

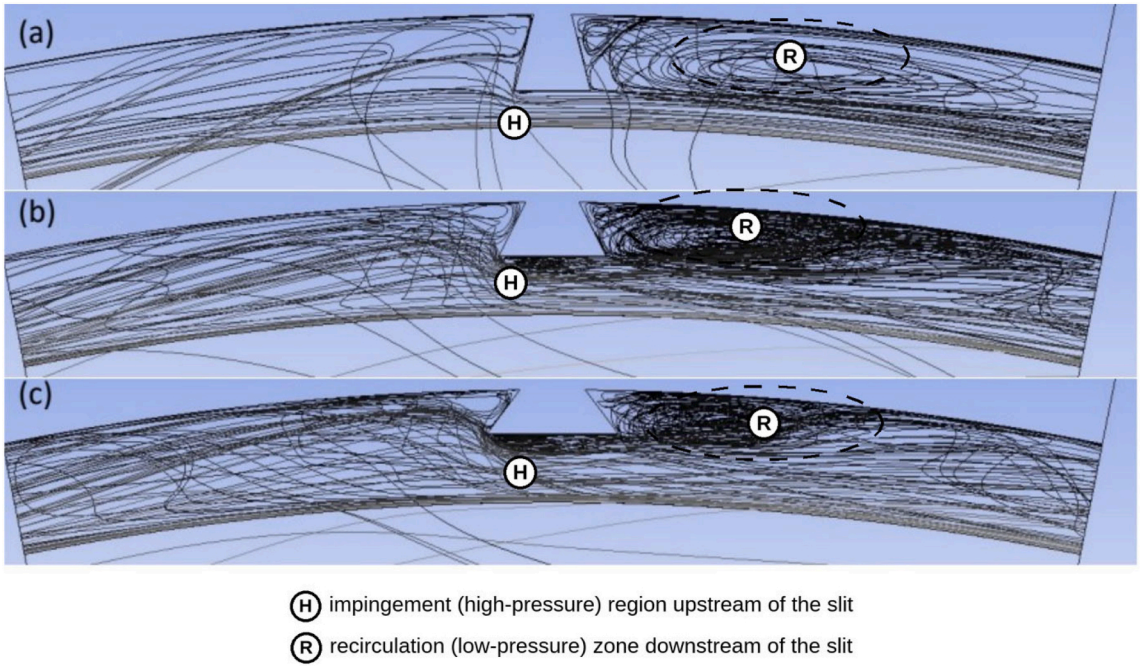


Fig. 15. The streamlines distribution of the FESS in X-Y plane for reversed trapezoid axial/inserted configuration under 1 bar pressure and rotational velocity of 1600 rad/s as a function of B/C ratio where: (a) 0.5, (b) 1, and (c) 1.5.

and it acts in the opposite direction.

The half-ellipse profile is the least favourable of the four in this respect. Its smooth curved leading face produces a weaker separation and a lower rate of turbulence production than the sharp edges of the

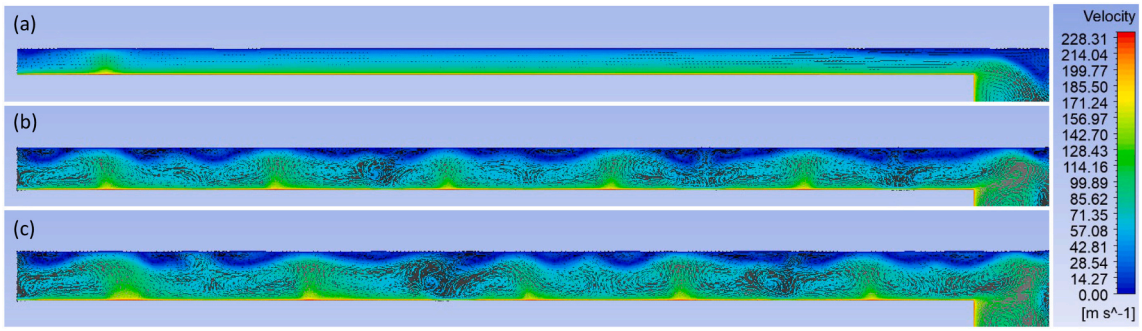


Fig. 16. Velocity contour of the FESS in Y-Z plane for reversed trapezoid shape under 1 bar pressure and rotational velocity of 1600 rad/s as a function of B/C ratio where: (a) 0.5, (b) 1, and (c) 1.5.

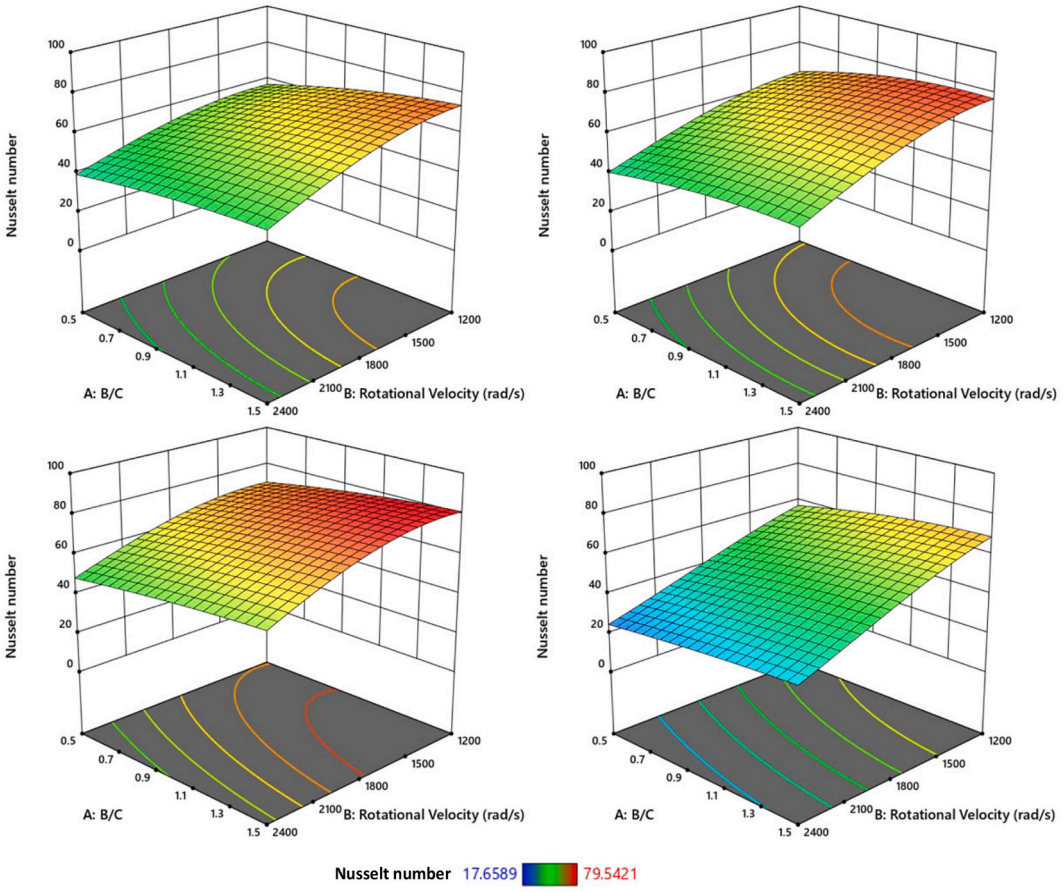


Fig. 17. 3D plot of Nusselt number for a half-ellipse shape as a function of factors D and E where: (a) radial/grooved, (b) radial/inserted, (c) axial/grooved, and (d) axial/inserted.

rectangular and trapezoidal profiles, which is precisely the property that makes it advantageous for windage loss, but reduces the momentum exchange for heat transfer once the cavity vortex has been disrupted. For the half-ellipse the Nusselt number in the inserted configuration is therefore lower than in the axial grooved configuration, notwithstanding the superior flow structure within the cavity. The two configurations are governed by different mechanisms, and the dead-zone argument applies to the grooved case alone; within that case the half-ellipse retains the highest Nusselt number of the four profiles examined.

As shown in Fig. 19, the collision of the mainstream fluid with the wall on the left side of the slit generates a region of elevated velocity, promoting enhanced mixing and heat exchange between fluid streams at differing temperatures. Within the slit, the fluid velocity progressively decreases along the rotational direction of the vortex due to the viscous and frictional forces imposed by the wall. This produces a low-velocity region along the right wall of the slit, where the mixing effect is reduced and a cooler temperature zone consequently develops. The extent of the high-velocity region is notably larger in the half-ellipse model than in the other configurations. This behaviour can be attributed to the distinctive geometric characteristics of the half-ellipse shape, which promote greater fluid-wall interaction, thereby strengthening the mixing and heat transfer processes between the fluid streams. The velocity contours of Fig. 19 are extracted from the same X–Y observation plane, and at the same axial and angular location, as the streamlines of Fig. 18. The vortex core marked V in Fig. 18 coincides with the low-velocity core marked V in Fig. 19, and the flow dead zones marked D

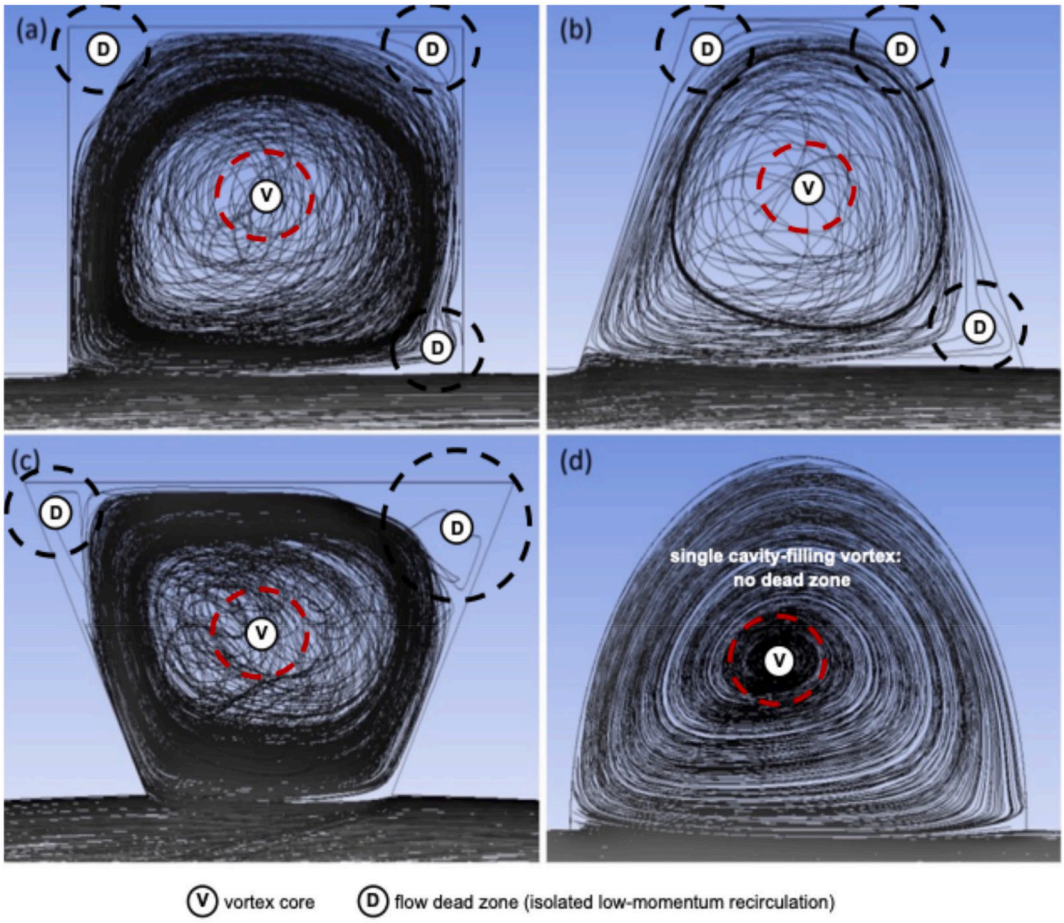


Fig. 18. The streamlines distribution of the FESS in X-Y plane for the axial/grooved configuration under 1 bar pressure and rotational velocity of 1600 rad/s for: (a) rectangle, (b) trapezoid, (c) reversed trapezoid, and (d) half-ellipse.

in Fig. 18 lie within the low-velocity, reduced-mixing, regions marked L in Fig. 19.

Fig. 20 presents the velocity contour within the airgap between the rotor and the housing along the Y-Z plane for the half-ellipse geometric configuration. The illustration demonstrates a progressive reduction in the number of Taylor vortices as the configuration transitions from (a) radial/grooved to (b) radial/inserted, followed by (c) axial/grooved, and finally (d) axial/inserted. In the axial/inserted configuration, Taylor vortices are notably absent, a consequence of the disruptive effect of the slit, which induces a backflow that effectively suppresses their formation. In the radial/inserted configuration, by contrast, the presence and number of slits play a significant role in governing the quantity of Taylor vortices. These vortices are confined to the regions between adjacent slits, with the slits acting as barriers that prevent the development of secondary vortices in the zones immediately adjacent to the rotor. This behaviour highlights the complex interaction between the structural geometry and the fluid dynamics operating within the system.

Fig. 21 presents the velocity contours for the radial grooved configuration across all slit geometries examined. It is observed that each slit shape promotes either the formation of secondary vortices within the slit cavity or allows a portion of the primary vortices to penetrate into the slit. This interaction enhances the mixing of hot and cold air streams, which is essential for effective thermal management. Fig. 22 illustrates the velocity vectors corresponding to the slit positions established in Fig. 21. It is evident that a slit may contain a single secondary vortex that circulates within it; however, this can give rise to flow dead zones, as previously discussed. Alternatively, when a slit accommodates two vortices that represent extensions of the primary vortices, these dead zones are mitigated, resulting in superior fluid mixing. The occurrence of secondary vortices within the slits is generally proportional to that of the primary vortices across all configurations, with the notable exception of the half-ellipse shape. In the case of the half-ellipse, a disproportionately greater number of secondary vortices is observed, as depicted in Fig. 21. This distinction highlights the unique fluid dynamic characteristics conferred by the half-ellipse geometry, and its consequent effect on the overall mixing efficiency of the system.

In pursuit of maximising the Nusselt number to enhance convective heat transfer between the rotor and the casing, a comprehensive investigation employing RSM was conducted, examining six influential factors. Several design and operational modifications have been identified as effective strategies for improving the Nusselt number. An increase in the B/C ratio has been found to produce a beneficial effect on heat transfer performance. Maintaining the rotational velocity within the range of 1200 to 1600 rad/s contributes positively, likely by enabling more stable and coherent heat transfer conditions at the fluid-wall interface. Increasing the pressure within the cavity represents an additional approach that intensifies the heat transfer coefficient, thereby elevating the Nusselt number. Orienting the slits in the axial direction aligns the flow with the prevailing thermal gradient, promoting more effective convective heat transfer. The adoption of a grooved configuration further increases the effective surface area and promotes turbulent mixing, both of which are conducive to heat transfer enhancement. Finally, the use of a half-ellipse slit shape has been demonstrated to be particularly effective in improving the Nusselt number across the configurations examined.

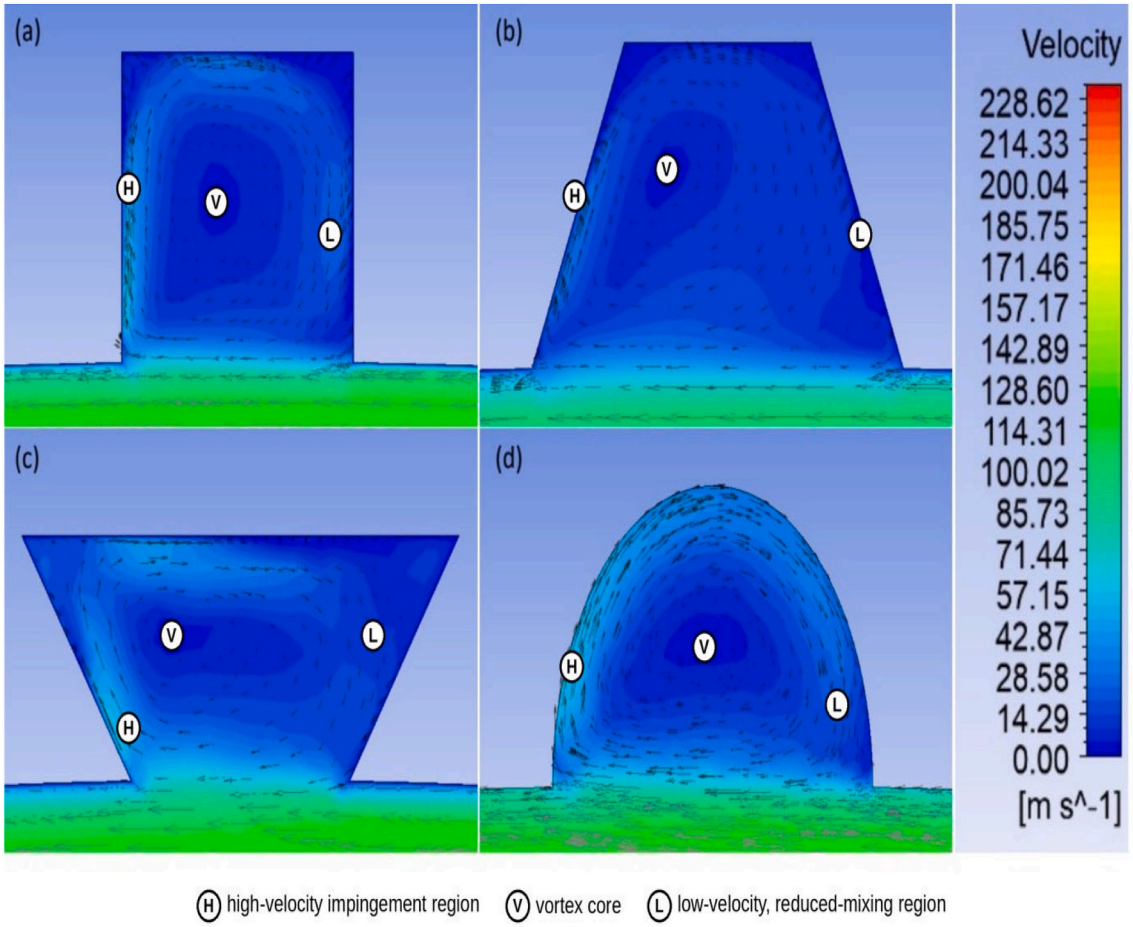


Fig. 19. Velocity contour of the FESS in X-Y plane for the axial/grooved configuration under 1 bar pressure and rotational velocity of 1600 rad/s for: (a) rectangle, (b) trapezoid, (c) reversed trapezoid, and (d) half-ellipse.

4.6. Optimisation

Myers and Montgomery [53] introduce the concept of "desirability" within the context of a multiple-response optimisation method. The desirability function, denoted as *D(X)*, serves as the objective function in this multi-criterion decision-making process. The function assigns a value within the range of zero to one to each response, where one indicates the highest desirability and zero represents conditions outside the desirable range. The composite objective function, which encapsulates the overall desirability, is constructed as the geometric mean of these individual transformed responses, as follows:

$$D = (d_1 \bullet d_2 \bullet \ldots d_n)^{\frac{1}{n}} = \left(\prod_{i=1}^{n} d_i\right)^{\frac{1}{n}} \tag{13}$$

Where n is the number of responses measured. This function transitions linearly from zero, outside the predetermined limits, to one at the target point. The maximisation of this desirability function is pursued through numerical optimisation techniques, wherein the relative importance of each objective can be weighted to influence the outcome. In this optimisation framework, a singular desirability function incorporates a spectrum of responses and variables. Utilising the Design-Expert software, numerical optimisation was performed to balance the system's responses accordingly. The software, considering the significance of each variable, provided multiple solutions to attain optimal desirability. The optimisation aimed to minimise windage losses while simultaneously maximising the Nusselt number, thereby achieving an ideal balance between fluid dynamics and heat transfer performance.

The predicted windage losses and Nusselt number for the proposed design were validated against CFD simulation results for each scenario to confirm the reliability of the predictions. The comparison demonstrates close agreement between the numerical simulations and the predicted values, with discrepancies of 3% in windage losses and 4% in the Nusselt number. All comparisons were conducted at a rotational velocity of 2400 rad/s, corresponding to the maximum rotor speed and representing the fully charged state of the flywheel.

Considering the dual objectives of minimising windage losses while simultaneously maximising the Nusselt number, the most favourable configuration was identified as a B/C ratio of 1.2, a pressure of 0.47 bar, axial slit direction, a grooved surface configuration, and a trapezoid slit shape. This configuration produced windage losses of 1467 W and a Nusselt number of 42. In contrast, when the optimisation objective is restricted to windage loss minimisation alone, the optimal design shifts to a B/C ratio of 1, a lower pressure of 0.2 bar, radial slit orientation, a grooved surface, and a reversed trapezoid slit shape, yielding considerably lower windage losses of 738 W, albeit with a reduced Nusselt number of 19. Conversely, when the sole objective is the maximisation of the Nusselt number, the design parameters adjust to a B/C ratio of 0.5, an elevated pressure of 1 bar, axial slit orientation, a grooved configuration, and a trapezoid slit shape, resulting in higher windage losses of 2147 W but a substantially improved Nusselt number of 59.

4.7. The effect of slits

This study examined the role of slit configurations in improving the performance of flywheel energy storage systems, with particular

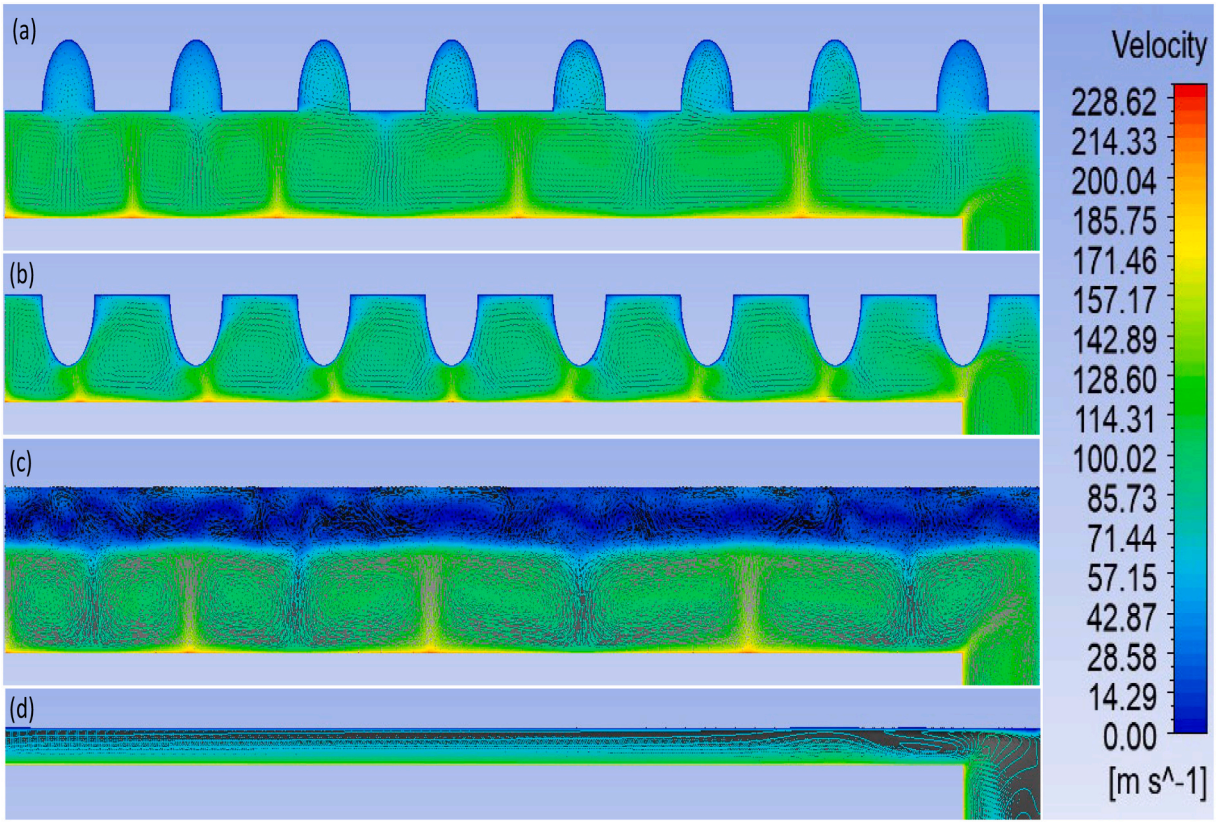


Fig. 20. Velocity contour of the FESS in Y-Z plane for half-ellipse shape under 1 bar pressure and rotational velocity of 1600 rad/s as a function of factors D and E where: (a) radial/grooved, (b) radial/inserted, (c) axial/grooved, and (d) axial/inserted.

emphasis on reducing windage losses and enhancing the Nusselt number. Using RSM, the study determined the most effective combinations of design variables, encompassing slit shape, orientation, configuration, pressure level, rotational velocity, and B/C ratio, to identify an optimal design solution. To assess the effectiveness of the optimised design, comparisons were drawn against a baseline model that was identical in all respects except for the absence of slits in the casing. This comparative approach was essential to isolate and quantify the specific contribution of the slit geometry to overall system performance.

The results of this comparison were notable. In the first scenario, targeting simultaneous optimisation of both windage losses and the Nusselt number, the slit-integrated design achieved an 8% reduction in windage losses and an 11% improvement in the Nusselt number relative to the baseline model. When the optimisation was directed exclusively towards windage loss reduction, the enhanced design delivered a 9% decrease in windage losses and, additionally, a 14% increase in the Nusselt number. In the third scenario, where the optimisation objective was focused on the Nusselt number alone, the optimised design still produced a 3% reduction in windage losses alongside a substantial 18% enhancement in the Nusselt number. These results collectively demonstrate that the strategic integration of slits into the casing design not only fulfils the intended optimisation objectives but also consistently produces concurrent benefits in terms of reduced windage losses and improved convective heat transfer, as quantified by the Nusselt number.

4.8. Manufacturing considerations

The optimisation presented above is formulated in terms of the two performance objectives alone and does not include manufacturing cost or complexity as an objective; the optimum configurations reported are therefore optimal with respect to windage loss and heat transfer, and the discussion that follows is intended to establish that they are also realisable by established manufacturing routes.

The first point to note is that the rotor is a plain solid cylinder in every configuration examined. No geometric modification is applied to the rotating component, and the entire geometric complexity resides in the stationary casing. This distinction is important since it is the rotor for which the requirements on dimensional tolerance, dynamic balance and material integrity are most severe at the peripheral speeds concerned, and for which any geometric modification would carry a substantial qualification burden. Leaving the rotor unmodified means that none of the modifications proposed here affect the burst margin, the balancing procedure or the certification of the rotating assembly.

The casing is machined from a solid block, which is the route already adopted in commercial flywheel units, including those manufactured by the industrial partner associated with the authors' previous experimental work [5]. Within this route the grooved configurations require only the removal of material from the bore and can be produced in a single set-up: by axial broaching or end milling for the axial orientation, and by internal circumferential grooving for the radial orientation. No additional components, joints or fasteners are introduced, and the slit array is formed in the same operation that finishes the bore.

Among the cross-sectional profiles, the rectangular and trapezoidal geometries are the most readily produced with standard tooling. The half-ellipse requires a profiled form tool or a controlled ball-nose milling path and is correspondingly more demanding, while the reversed trapezoid, whose cross-section widens with increasing distance from the bore surface, forms an undercut that cannot be generated by simple plunge or end milling and requires a T-slot or dovetail cutter. The conclusions relating to the half-ellipse should therefore be understood as identifying the upper bound of thermal performance attainable by a casing with slits. Where cost is the binding constraint, the trapezoidal grooved configuration identified as the multi-objective optimum delivers the greater part of the available benefit at a substantially lower

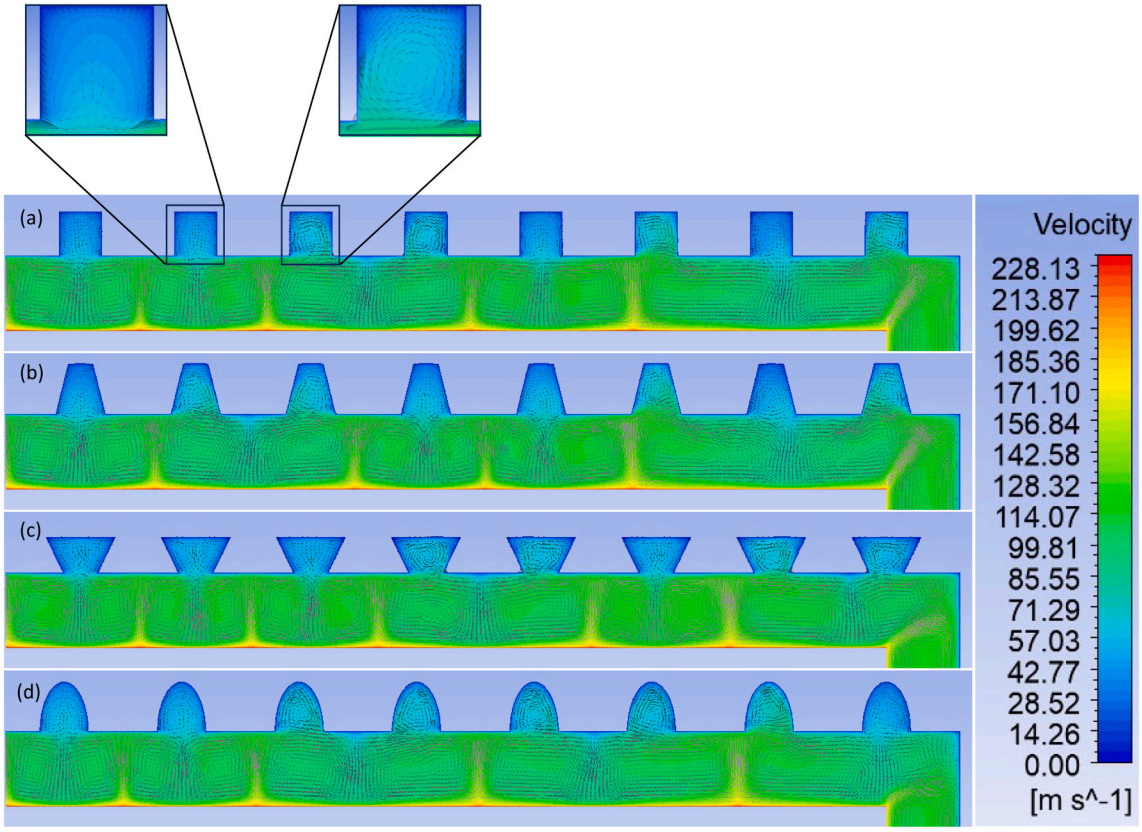


Fig. 21. Velocity contour of the FESS in Y-Z plane for the radial/grooved configuration under 1 bar pressure and rotational velocity of 1600 rad/s for: (a) rectangle, (b) trapezoid, (c) reversed trapezoid, and (d) half-ellipse.

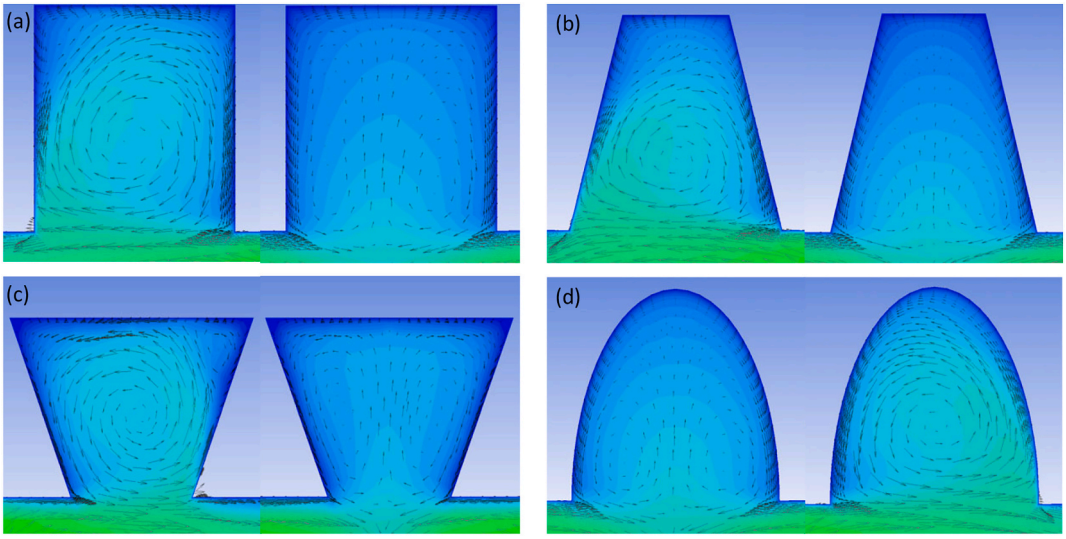


Fig. 22. Velocity contour of the slit in Y-Z plane for the radial/grooved configuration under 1 bar pressure and rotational velocity of 1600 rad/s for: (a) rectangle, (b) trapezoid, (c) reversed trapezoid, and (d) half-ellipse.

manufacturing complexity.

5. Conclusion

This research has investigated the effects of slit geometries on the performance of FESS through a comprehensive numerical study utilising RSM. To determine the validity of the CFD results, model validation was performed, which revealed a good agreement between the numerical and experimental data. Reducing windage losses in FESS can be achieved by optimising slit dimensions, decreasing rotational velocity, lowering cavity pressure, aligning slits radially, adopting a grooved configuration, and utilising a reversed trapezoid geometry to minimise skin friction coefficient. To achieve the highest Nusselt number within the FESS, a combination of factors, including increasing the base to height length (B/C) ratio, maintaining rotational velocity within 1200 to 1600 rad/s, raising cavity pressure, orienting slits axially, implementing

a grooved configuration, and adopting a half-ellipse component shape. The findings have revealed that slit inclusion can effectively minimise windage losses and enhance heat transfer rates, simultaneously optimising both key performance indicators. Comparative evaluations against a base model revealed that the slit-enhanced design consistently outperformed the conventional design in all scenarios. For instance, the optimised design achieved an 8% reduction in windage losses and an 11% increase in the Nusselt number compared to the base model when both parameters were optimised simultaneously. The optimisation was performed, with numerical values in good agreement with the model predictions. The critical contribution of this work is studying the relationships and effects of various parameters on the performance of flywheel energy storage, which offer valuable insights for improving FESS efficiency, reliability, and longevity, while also contributing to broader sustainable energy goals. The configurations identified as optimal are realised by machining the casing bore alone, leaving the rotor geometrically unmodified, and are therefore compatible with the manufacturing route already employed for commercial flywheel housings. Since the reductions reported here were achieved under moderate sub-atmospheric and ambient pressure conditions, the results further suggest that a portion of the windage losses traditionally mitigated through high-vacuum operation can instead be reduced through geometric design optimisation. This finding indicates that the sealing and vacuum requirements of the containment system may be relaxed while still preserving the rotor's convective cooling pathway.

CRediT authorship contribution statement

Mahmoud Eltaweel: Writing – review & editing, Writing – original draft, Visualization, Validation, Software, Resources, Methodology, Investigation, Conceptualization, Formal analysis. **Mohammad Reza Herfatmanesh:** Writing – review & editing, Supervision, Resources, Project administration, Funding acquisition, Conceptualization.

Declaration of competing interest

The authors declare that they have no known competing financial interests or personal relationships that could have appeared to influence the work reported in this paper.

Acknowledgements

This work is supported by the European Union‘s Horizon 2020 research and innovation programme under the Marie Skłodowska-Curie grant agreement No 801604.

Data availability

Data will be made available on request.

References

[1] A.Z.A. Shaqsi, K. Sopian, A. Al-Hinai, Review of energy storage services, applications, limitations, and benefits, Energy Rep. 6 (2020) 288–306.
[2] A.G. Olabi, T. Wilberforce, M.A. Abdelkareem, M. Ramadan, Critical review of flywheel energy storage system, Energies 14 (8) (2021) 2159.
[3] G. Genta, Kinetic energy storage: theory and practice of advanced flywheel systems, Butterworth-Heinemann, 1985.
[4] X. Li, A. Palazzolo, A review of flywheel energy storage systems: state of the art and opportunities, J. Energy Storage 46 (2022) 103576.
[5] S. Motaman, M. Eltaweel, M.R. Herfatmanesh, T. Knichel, A. Deakin, Numerical analysis of a flywheel energy storage system for low carbon powertrain applications, J. Energy Storage 61 (2023) 106808, https://doi.org/10.1016/j.est.2023.106808.
[6] E. Gundabattini, R. Kuppan, D.G. Solomon, A. Kalam, D. Kothari, R.A. Bakar, A review on methods of finding losses and cooling methods to increase efficiency of electric machines, Ain Shams Eng. J. 12 (1) (2021) 497–505.
[7] S. Li, S. Zhang, T.G. Habetler, R.G. Harley, Modeling, design optimization, and applications of switched reluctance machines—A review, IEEE Trans. Ind. Appl. 55 (3) (2019) 2660–2681.
[8] M.E. Amiryar, K.R. Pullen, Analysis of standby losses and charging cycles in flywheel energy storage systems, Energies 13 (17) (2020) 4441.
[9] A. Nouri-Borujerdi, M. Nakhchi, Heat transfer enhancement in annular flow with outer grooved cylinder and rotating inner cylinder: Review and experiments, Appl. Therm. Eng. 120 (2017) 257–268.
[10] S. Sun, D. Liu, Y.-Z. Wang, S.M.R.S. Naqvi, H.-B. Kim, Heat transfer characteristics of Taylor–Couette flow with axially distributed slits using field synergy principle and entropy generation analysis, Int. Commun. Heat Mass Transfer 129 (2021) 105699.
[11] S. Sun, D. Liu, W.-D. Shi, Y.-Z. Wang, H.-B. Kim, Numerical Simulations of Heat Transfer Performance of Taylor–Couette Flow in Slit Model, Arab. J. Sci. Eng. 46 (2021) 7153–7170.
[12] T. Tsukahara, M. Ishikawa, Y. Kawaguchi, DNS study of the turbulent Taylor-Vortex flow on a ribbed inner cylinder, Adv. Mech. Eng. 5 (2013) 628490.
[13] S. Gokul, M. Deepu, Fluid flow and heat transfer in an annulus with ribs on the rotating inner cylinder surface, J. Therm. Sci. Eng. Appl. 12 (4) (2020) 041026.
[14] S.-C. Tzeng, W.-P. Ma, C.-W. Lin, W.-Y. Jywe, C.-H. Liu, Y.-C. Wang, Experimental investigation of lubrication and cooling effects of high-speed rotating machines, Int. J. Adv. Manuf. Technol. 35 (2007) 394–399.
[15] D. Liu, S. Ding, W. Zhou, S. Sun, H. Kim, Turbulent Taylor–Couette flow and its heat transfer characteristic based on PANS model, J. Drain. Irrig. Mach. Eng. 37 (10) (2019) 889–894.
[16] D. Liu, M.I.A. Mohammedsalih, A.-G.N. Kofi, N.K. Amponsah-Gyenin, S. Ding, S. Sun, Numerical study of heat flow characteristics of turbulent Taylor-Couette flow in slit wall model, J. Eng. Res. 10 (1B) (2022) 312–331.
[17] D. Liu, C. Chao, Y. Wang, F. Zhu, H.-B. Kim, Axial slit wall effect on the flow instability and heat transfer in rotating concentric cylinders, J. Mech. Sci. Technol. 30 (2016) 5513–5519.
[18] Y. Sommerer, G. Lauriat, Numerical study of steady forced convection in a grooved annulus using a design of experiments, J. Heat Transf. 123 (5) (2001) 837–848.
[19] X. Zhu, R. Ostilla-Mónico, R. Verzicco, D. Lohse, Direct numerical simulation of Taylor–Couette flow with grooved walls: torque scaling and flow structure, J. Fluid Mech. 794 (2016) 746–774.
[20] D. Liu, Y. Qi, S. Sun, Y.-Z. Wang, Numerical investigation of flow and heat transfer between concentric cylinders with slit wall, Case Stud. Therm. Eng. 22 (2020) 100783.
[21] K. Bilen, M. Cetin, H. Gul, T. Balta, The investigation of groove geometry effect on heat transfer for internally grooved tubes, Appl. Therm. Eng. 29 (4) (2009) 753–761.
[22] D. Lorenzini-Gutierrez, A. Hernandez-Guerrero, J.L. Luviano-Ortiz, J.C. Leon-Conejo, Numerical and experimental analysis of heat transfer enhancement in a grooved channel with curved flow deflectors, Appl. Therm. Eng. 75 (2015) 800–808.
[23] J. Liu, G. Xie, T.W. Simon, Turbulent flow and heat transfer enhancement in rectangular channels with novel cylindrical grooves, Int. J. Heat Mass Transf. 81 (2015) 563–577.
[24] F. Tachibana, S. Fukui, Convective heat transfer of the rotational and axial flow between two concentric cylinders, Bull. JSME 7 (26) (1964) 385–391.
[25] S.-H. Lee, H.-T. Chung, C.-W. Park, H.-B. Kim, Experimental investigation of the effect of axial wall slits on Taylor–Couette flow, Fluid Dyn. Res. 41 (4) (2009) 045502.
[26] S. Eiamsa-ard, P. Promvonge, Thermal characteristics of turbulent rib-grooved channel flows, Int. Commun. Heat Mass Transfer 36 (7) (2009) 705–711, https://doi.org/10.1016/j.icheatmasstransfer.2009.03.025.
[27] A. Nouri-Borujerdi, M. Bovand, S. Rashidi, K. Dincer, Geometric parameters and response surface methodology on cooling performance of vortex tubes, Int. J. Sustain. Energy 36 (9) (2017) 872–886, https://doi.org/10.1080/14786451.2015.1127233.
[28] L.O. Salviano, D.J. Dezan, J.I. Yanagihara, Optimization of winglet-type vortex generator positions and angles in plate-fin compact heat exchanger: response surface methodology and direct optimization, Int. J. Heat Mass Transf. 82 (2015) 373–387.
[29] A. Nouri-Borujerdi, M. Nakhchi, Optimization of the heat transfer coefficient and pressure drop of Taylor-Couette-Poiseuille flows between an inner rotating cylinder and an outer grooved stationary cylinder, Int. J. Heat Mass Transf. 108 (2017) 1449–1459.
[30] B. Andersson, R. Andersson, L. Håkansson, M. Mortensen, R. Sudiyo, B. Van Wachem, Computational fluid dynamics for engineers, Cambridge university press, 2011.
[31] N. Regalado-Rodríguez, C. Militello, Comparative study of the effects of increasing heat transfer area within compression and expansion chambers in combination with modified pistons in Stirling engines. A simulation approach based on CFD and a numerical thermodynamic model, Energy Convers. Manag. 268 (2022) 115930.
[32] J. Tu, G.H. Yeoh, C. Liu, Chapter 3 - Governing Equations for CFD—Fundamentals, in: J. Tu, G.H. Yeoh, C. Liu (Eds.), Computational Fluid Dynamics, Butterworth-Heinemann, Burlington, 2008, pp. 65–125, https://doi.org/10.1016/B978-075068563-4.50005-7.
[33] W.M. Rohsenow, J.P. Hartnett, Y.I. Cho, Handbook of heat transfer 3, Mcgraw-hill New York, 1998.
[34] N.G. Hadjiconstantinou, The limits of Navier-Stokes theory and kinetic extensions for describing small-scale gaseous hydrodynamics, Phys. Fluids 18 (11) (2006) 111301.
[35] H.-P. Liu, M. Werst, J.J. Hahne, D. Bogard, Prediction of windage losses of an enclosed high speed composite rotor in low air pressure environments, presented at the, Heat Transfer Summer Conference, 2003, pp. 15–23.

[36] G.I. Taylor, VIII. Stability of a viscous liquid contained between two rotating cylinders, Philosophical Transactions of the Royal Society of London. Series A, Containing Papers of a Mathematical or Physical Character 223 (605–615) (1923) 289–343.
[37] P. Reinke, M. Schmidt, T. Beckmann, The cavitating Taylor-Couette flow, Phys. Fluids 30 (10) (2018) 104101.
[38] C. Gazley Jr., Heat-transfer characteristics of the rotational and axial flow between concentric cylinders, Trans. Am. Soc. Mech. Eng. 80 (1) (1958) 79–89.
[39] K.M. Becker, J. Kaye, Measurements of diabatic flow in an annulus with an inner rotating cylinder, J. Heat Transf. (1962) 97–104, https://doi.org/10.1115/1.3684335.
[40] K. Ryu, K.-S. Lee, Generalized heat-transfer and fluid-flow correlations for corrugated louvered fins, Int. J. Heat Mass Transf. 83 (2015) 604–612.
[41] J.D. Anderson, J. Wendt, Computational fluid dynamics 206, Springer, 1995.
[42] C. Jungreuthmayer, et al., A detailed heat and fluid flow analysis of an internal permanent magnet synchronous machine by means of computational fluid dynamics, IEEE Trans. Ind. Electron. 59 (12) (2011) 4568–4578.
[43] K.R. Anderson, J. Lin, C. McNamara, V. Magri, CFD study of forced air cooling and windage losses in a high speed electric motor, J. Electron. Cool. Therm. Control. 5 (02) (2015) 27.
[44] A. Nachouane, A. Abdelli, G. Friedrich, S. Vivier, Estimation of windage losses inside very narrow air gaps of high speed electrical machines without an internal ventilation using CFD methods, presented at the 2016 XXII International Conference on Electrical Machines (ICEM), IEEE, 2016, pp. 2704–2710.
[45] D.A. Howey, A.S. Holmes, K.R. Pullen, Measurement and CFD prediction of heat transfer in air-cooled disc-type electrical machines, IEEE Trans. Ind. Appl. 47 (4) (2011) 1716–1723.
[46] M.L. Hosain, R.B. Fdhila, K. Rönnberg, Taylor-Couette flow and transient heat transfer inside the annulus air-gap of rotating electrical machines, Appl. Energy 207 (2017) 624–633.
[47] H. Reichardt, Über die Geschwindigkeitsverteilung in einer geradlinigen turbulenten Couetteströmung, *Z. Angew. Math. Mech.* 36 (S1) (1956) S26–S29.
[48] T. Tatsumi, Turbulence as a complex mechanical-system, Appl. Energy 67 (1–2) (2000) 91–116.
[49] H. Aoki, H. Nohira, H. Arai, Convective heat transfer in an annulus with an inner rotating cylinder, Bull. JSME 10 (39) (1967) 523–532.
[50] R. Donnelly, Experiments on the stability of viscous flow between rotating cylinders I. Torque measurements, Proc. R. Soc. Lond. Ser. Math. Phys. Sci. 246 (1246) (1958) 312–325.
[51] Y. Han, Z. Ren, Y. Tong, General Design Method of Flywheel Rotor for Energy Storage System, *2012 Int.* Conf. Future Energy Environ. Mater. 16 (2012) 359–364, https://doi.org/10.1016/j.egypro.2012.01.059.
[52] M. Fénot, Y. Bertin, E. Dorignac, G. Lalizel, A review of heat transfer between concentric rotating cylinders with or without axial flow, Int. J. Therm. Sci. 50 (7) (2011) 1138–1155.
[53] R.H. Myers, D.C. Montgomery, C.M. Anderson-Cook, Response surface methodology: process and product optimization using designed experiments, John Wiley & Sons, 2016.